

A semi-empirical method for estimating complete surface temperature from radiometric surface temperature, a study in Hong Kong city

Yang, Jinxin; Wong, Man Sing; Ho, Hung Chak; Krayenhoff, E. Scott; Chan, P. W.; Abbas, Sawaid; Menenti, Massimo

DOI

[10.1016/j.rse.2019.111540](https://doi.org/10.1016/j.rse.2019.111540)

Publication date

2020

Document Version

Accepted author manuscript

Published in

Remote Sensing of Environment

Citation (APA)

Yang, J., Wong, M. S., Ho, H. C., Krayenhoff, E. S., Chan, P. W., Abbas, S., & Menenti, M. (2020). A semi-empirical method for estimating complete surface temperature from radiometric surface temperature, a study in Hong Kong city. *Remote Sensing of Environment*, 237, Article 111540. <https://doi.org/10.1016/j.rse.2019.111540>

Important note

To cite this publication, please use the final published version (if applicable).
Please check the document version above.

Copyright

Other than for strictly personal use, it is not permitted to download, forward or distribute the text or part of it, without the consent of the author(s) and/or copyright holder(s), unless the work is under an open content license such as Creative Commons.

Takedown policy

Please contact us and provide details if you believe this document breaches copyrights.
We will remove access to the work immediately and investigate your claim.

**A semi-empirical method for estimating complete surface temperature from
radiometric surface temperature, a study in Hong Kong city**

Jinxin Yang^{1,2}, Man Sing Wong^{2*}, Hung Chak Ho^{2,3}, E. Scott Krayenhoff⁴, PW
Chan⁵, Sawaid Abbas², Massimo Menenti^{6,7}

¹School of Geographical Science, Guangzhou University, Guangzhou 510275, China,
yangjx11@gzhu.edu.cn

²Department of Land Surveying and Geo-Informatics, The Hong Kong Polytechnic
University, Kowloon, Hong Kong; email: lswong@polyu.edu.hk

³Department of Urban Planning and Design, The University of Hong Kong, Hong
Kong; hcho21@hku.hk

⁴School of Environmental Sciences, University of Guelph, Guelph, ON, Canada,
skrayenh@uoguelph.ca

⁵Hong Kong Observatory, Hong Kong, pwchan@hko.gov.hk

⁶Faculty of Civil Engineering and Earth Sciences, Delft University of Technology,
P. O. Box 5048, 2600 GA Delft, Netherlands; e-mail: m.menenti@tudelft.nl

⁷State Key Laboratory of Remote Sensing Science, Institute of Remote Sensing and
Digital Earth, Chinese Academy of Sciences, Beijing 100101, PR China

19 SYMBOLS and ACRONYMS:

20 T_c - complete surface temperature (K)

21 T_r - radiometric temperature from nadir view direction (K)

22 TUF-3D - Temperatures of Urban Facets in 3D

23 λ_p - planar area index

24 F - wall facet area index

25 ASTER - Advanced Spaceborne Thermal Emission and Reflection Radiometer

26 TM - Landsat Thematic Mapper

27 UST - urban surface temperature (K)

28 LASER/F-LAtent, SEnsible, Radiation Fluxes

29 Kn - solar radiation above urban canopy (W/m^2)

30 θ_a - solar azimuth angle ($^\circ$)

31 θ_z - solar zenith angle ($^\circ$)

32 T_{roof} - roof temperature (K)

33 T_{road} - road temperature (K)

34 T_{wall} - wall temperature (K)

35 L_r - radiation at the bottom of atmosphere at nadir view modeled by TUF-3D (W/m^2)

36 ε - emissivity

37 σ - Stefan–Boltzmann constant ($5.6703 \times 10^{-8} \text{ W m}^{-2} \text{ K}^{-4}$)

38 L_d - downwelling atmospheric radiation

39 $E(i)$ - radiance leaving urban canopy of pixel i ($\text{W} \cdot \text{m}^{-2} \cdot \text{sr}^{-1} \cdot \mu\text{m}^{-1}$)

40 $R_{at\uparrow}$ - downward atmospheric thermal radiance ($\text{W} \cdot \text{m}^{-2} \cdot \text{sr}^{-1} \cdot \mu\text{m}^{-1}$)

Abstract

The complete surface temperature (T_c) in urban areas, defined as the mean temperature of the total active surface area, is an important variable in urban micro-climate research, specifically for assessment of the urban surface energy balance. Since most vertically-oriented building facets are not observed by a nadir-viewing remote imaging radiometer, the radiometric surface temperature (T_r) measured at a specific view angle cannot be used with existing heat transfer equations to estimate radiative and convective fluxes in the urban environment. Thus, it is necessary to derive T_c for city neighborhoods. This study develops a simple method to estimate T_c from T_r with the aid of the Temperatures of Urban Facets in 3D (TUF-3D) numerical model, which calculates 3-D sub-facet scale urban surface temperatures for a variety of surface geometries and properties, weather conditions and solar angles. The effects of geometric and meteorological characteristics – e.g., building planar area index (λ_p), wall facet area index (F), solar irradiance – on the difference between T_c and T_r were evaluated using the TUF-3D model. Results showed the effects of geometric and meteorological characteristics on the difference between T_c and T_r differ between daytime and nighttime. The study then sought to predict the relationship between T_r and T_c , using λ_p , F , and solar irradiance for daytime and only using λ_p and F for nighttime. Based on the simulated data from TUF-3D, the resulting relationships achieve a coefficient of determination (r^2) of 0.97 and a RMSE of 1.5 K during daytime, with corresponding nighttime values of $r^2 = 0.98$ and RMSE = 0.69 K. The relationships between T_r and T_c are evaluated using high resolution airborne thermal

images of daytime urban scenes: $r^2 = 0.75$ and RMSE = 1.09 K on August 6, 2013 at 12:40 pm; and $r^2 = 0.86$ and RMSE = 1.86K on October 24, 2017 at 11:30 am. The new relationships were also applied to estimate T_c from T_r in Hong Kong retrieved from Landsat 5 Thematic Mapper (TM) and the Advanced Spaceborne Thermal Emission and Reflection Radiometer (ASTER). In the present climatic context, the difference between T_c and T_r can reach 10 K during daytime in summer, and 6 K during daytime in winter, with seasonal variation attributable to the variations in shortwave irradiance. The nighttime difference between T_c and T_r can also reach 2 K in both summer and spring seasons.

Keywords: remote sensing, surface temperature, thermal heterogeneity, urban geometry

1. Introduction

Background. Urban Surface Temperature (UST) is a key variable for studying urban surface energy exchange and microclimate in an urban environment (Arnfield, 2003; Arnfield and Grimmond, 1998; Cheng et al., 2010; Morrison et al., 2018; Nazarian et al., 2018a; Oke, 1988; Voogt and Oke, 2003; Yaghoobian et al., 2010). Satellite-based thermal infrared (TIR) data have been used for studying urban surface temperature and provide information at different temporal and spatial scales (Li et al., 2013), thus surface temperature from remote sensing data has been widely applied in urban climate research (Dousset and Gourmelon, 2003; Roth et al., 1989; Voogt and Oke, 2003; Weng, 2009). Most space-borne imaging radiometers observe terrestrial

targets in a close to nadir view direction and, therefore, can capture only horizontal facets. Thus, active radiation sources would be incompletely observed over urban areas (Adderley et al., 2015; Jiang et al., 2018; Roth et al., 1989). Theoretically, off-nadir-view satellite sensors can observe the vertical walls, but only a few multi-angle sensors provide off-nadir image data with thermal infrared spectral range, and such satellite images (e.g. Sea and Land Surface Temperature Radiometer (SLSTR) on-board Sentinel 3, ATSR-series) are with low spatial resolution (1km), which is not capable to be used over high-density urban environment. For densely built areas, active radiation sources are much larger than the horizontal area due to the large surface area of vertical facets (Roth et al. 1989). It is therefore challenging to retrieve urban surface temperature accurately and without large bias using thermal infrared remote sensing (Jiang et al., 2018).

In terms of the urban energy balance, convective heat transfer is often influenced by the complete surface of each roughness element. Thus, a representative surface temperature of the complete and 3D surface-atmosphere interface should be estimated since these temperatures contribute to the local heat exchange (Kanda et al., 2007; Kanda et al., 2005; Voogt and Oke, 1997). Voogt and Oke (1997) proposed the concept of the complete urban surface temperature (T_c), defined as weighted summation of the component surface temperatures, multiplied by the associated component fractions from a three-dimensional perspective. Compared with the radiometric surface temperature directly captured by a nadir-viewing remote imaging radiometer, T_c can provide superior information towards understanding urban climate.

Voogt and Oke (1997) compared sensible heat fluxes calculated from air temperature and different surface temperatures, and their results showed that the complete surface temperature should be used for the estimation of sensible heat flux in urban areas. In order to consider its significant implications in urban climate research, researchers have attempted to calculate T_c from remote sensing or field measurements (Allen et al., 2018; Jiang et al., 2018; Voogt and Oke, 1997). Voogt and Oke (1997) calculated T_c based on field measurement by a thermal camera data and digitizing building data from high-resolution (1:2500) aerial photography. Their results showed that there is a significant difference between T_c and the nadir T_r . Allen et al. (2018) calculated T_c from the hemispherical T_r measured by pyrgeometers and results showed that the difference between T_c and the temperature observed from a nadir view is up to 8 K under clear-sky viewing conditions. Jiang et al. (2018) estimated T_c from directional radiometric temperature based on simulated data from urban micro-climate model and remote sensing observation model, without ancillary ground-based data. They indicated that the estimation of T_c could be further improved by using radiometric temperatures observed at multiple view-angles.

Gaps in knowledge. The aforementioned studies estimated the T_c using field measurements or airborne data, while the estimation of T_c from satellite remote sensing data is still challenging due to their relatively low spatial resolution and to the thermal heterogeneity within the mixed pixels, which include roof and road facets with different temperatures. Since radiometric temperature is more readily available from satellite images than T_c , this study proposes a simple method to estimate T_c from

nadir observations of radiometric temperature view (T_r). A nadir viewing imaging radiometer can only observe the radiance emitted by horizontal facets and reflected by horizontal facets from facets around and atmosphere. The temperature of horizontal facets is also affected by vertical walls due to the radiative transfer and energy exchange between vertical walls and road surfaces (Nazarian and Kleissl, 2015; Yang and Li, 2015). Thus, T_r is related to wall temperatures and related to T_c to some extent. T_r and T_c are correlated with the building height, density of building, material and local climatic conditions. Buildings in a city have influences on the radiative and convective transfer and imply energy exchange of the wall facets with ambient atmosphere, which results in the spatial variability of urban surface temperature. In addition, shadows cast by buildings affect the variability of surface temperatures. For homogeneous or “pure” pixels, T_r and T_c are more or less identical, while thermally heterogeneous pixels in urban spaces are always affected by the complexity of urban surfaces, including building density, aspect ratio (ratio of building height to the street width), and material properties which contribute differently to energy exchange. Thus, the relationships between T_r and T_c can be parameterized by urban structural parameters (e.g. building density, building height) and local meteorological parameters. In order to develop the relationships, complex energy exchange within mixed pixels with high heterogeneity of urban surface temperature should be modeled.

The Temperatures of Urban Facets in 3D (TUF-3D) numerical model was adopted and used in this study to simulate T_r and T_c (Krayenhoff and Voogt, 2007).

TUF-3D provides (sub-) facet surface temperatures based on sub-facet scale solutions to the surface energy balance. The T_c can also be calculated therefore, by combining the facet surface temperatures provided by TUF-3D with the associated facet areas. T_r is provided by TUF-3D in order to represent a sensor viewing from a nadir direction, and it is calculated from the radiation emitted and reflected by roofs and roads.

Objectives. In order to estimate T_c from T_r , this study explored and established a relationship between T_c and T_r in a thermally heterogeneous environment with the use of numerical experiments based on TUF-3D and urban building structure parameters (Planar Area Index (λ_p) and Wall Facet area index (F)). The objectives of this study were 1) to assess the effects of urban building geometric parameters (e.g. λ_p , F) and local meteorological conditions (e.g. wind speed, solar radiation) on the relationship between T_c and T_r ; and 2) to evaluate the relationship between T_c and T_r using an urban energy balance model and numerical experiments and develop a simple method that uses T_r to retrieve T_c in a thermally heterogeneous urban environment. Subsequently, the developed method is used to estimate T_c from radiometric surface temperature observed by satellite data of the Landsat 5 Thematic Mapper (TM) with 30 m spatial resolution in daytime and Advanced Spaceborne Thermal Emission and Reflection Radiometer (ASTER) with 90 m spatial resolution in nighttime.

The study is organized as follows. After an Introduction structured in two sub-sections to articulate our problem statement, the objectives are stated, followed by a detailed presentation of the Methodology structured in five sub – sections, to describe

separately a sensitivity analysis and the design of numerical experiments from the development of a simple model to estimate T_c from T_r . Next, the data applied in the study are described by type, i.e. radiometric data acquired by satellites, digital surface models and meteorological data. The presentation of results mirrors the structure of the Methodology and is followed by a detailed Discussion. Lastly, the section of Conclusions is presented.

2. Methodology

2.1 General

In this study, a simple method is developed to estimate the complete surface temperature T_c from remote sensing measurements of the radiometric surface temperature T_r for daytime and nighttime respectively. For daytime, the method is based on a relationship f_d :

$$T_c = f_d(T_r, \lambda_p, F, Kn, \theta_a, \theta_z) \quad (1)$$

where T_r is the nadir radiometric temperature (K), λ_p is the planar area index, F is the wall facet area index, Kn is the down-welling solar irradiance at the top of the urban canopy (W/m^2), θ_a is the solar azimuth angle ($^\circ$), and θ_z is the solar zenith angle ($^\circ$). λ_p , defined as the ratio of plan area of buildings to the area of building footprint, is related to the building density. Specifically, λ_p is defined as the ratio of building total planar area to the area of the horizontal plane section of the building at ground level. The building footprint is the area of the horizontal plane section of the building at

ground level. The wall facet area index (F), calculated as the ratio of the wall facet area to the area of building footprint which contains the building and the road around it, is related to the building density and aspect ratio. λ_p is related to the directional temperature observed by remote sensing from nadir direction. F is related to the fraction unobserved by remote sensing. Thus, F and λ_p were used in this study as the building structure parameters to study the difference between T_c and T_r .

Fewer variables and parameters are taken into account during nighttime since the solar effects can be neglected at nighttime and the relationship between T_c and T_r becomes:

$$T_c = f_n(T_r, \lambda_p, F) \quad (2)$$

To construct our simple model, we used a large number of numerical experiments (see Sect. 2.3 for details) by TUF 3D (Krayenhoff and Voogt, 2007) to generate the pseudo – observations required to determine the relationships Eq.1 and 2. Considering that the solar effects would continue about 3 hours after sunset, the daytime numerical experiments from 8:00 am until 5:00 pm and the nighttime numerical experiments from 9:00 pm until 5:00 am were used for studying the relationships in Eqs. 1 and 2 between T_c and T_r .

Our study was limited to the built-up area where the fractional abundance of vegetation is negligible, so that the temperature of vegetation is not considered in this study. This is also aligned with our estimation in the TUF-3D model. The T_c was calculated using the facet temperatures (roof temperature T_{roof} , road temperature

212 T_{road} and wall temperature T_{wall}) and the facet area weights extracted from the TUF-
 213 3D output:

$$214 \quad T_c = \frac{T_{roof} * \lambda_p + T_{road} * (1 - \lambda_p) + T_{wall} * F}{1 + F} \quad (3)$$

215 T_r was calculated from the area-weighted average of upwelling radiation from
 216 roof and road facets according to the definition given by (Becker and Li, 1995). Since
 217 satellite sensors have narrow fields of view, only the roof and road facets are observed
 218 from a nadir view. The upwelling radiation includes the emitted radiation by roof and
 219 road facet and the radiation emitted by wall facets and atmosphere, then reflected by
 220 roof and road facets. The reflected radiation depends on the wall surface temperature
 221 and material emissivities of walls and roads as well as the sensor-ground geometry. In
 222 this study, we only consider the nadir radiometric temperature. In the TUF – 3D
 223 domain, we obtained the T_r from the radiation at the bottom of atmosphere L_r
 224 captured by the pseudo – observations collected by a fictive nadir – viewing imaging
 225 radiometer placed:

$$L_r = \varepsilon \sigma T_r^4 + (1 - \varepsilon) L_d \quad (4)$$

226 ε is calculated as the area-weighted average of roof and road emissivities. σ is the
 227 Stefan–Boltzmann constant ($5.6703 \times 10^{-8} \text{ Wm}^{-2}\text{K}^{-4}$). L_d is the downwelling
 228 atmospheric radiation, T_r is the radiometric temperature measured by a fictive nadir-
 229 viewing remote radiometer. The TUF-3D provides the upwelling radiation from
 230 road and roof which includes the radiation emitted by roof and road facets and the
 231 radiation emitted by wall facets and by the atmosphere and reflected by roof and road
 232 facets. Then the L_r can be calculated as the area weighted average of roof and road
 233 facets. L_d is calculated from the atmospheric profile in TUF-3D.

234 The design of the numerical experiments is described in Sect. 2.3. The variables

and parameters in the Eq.1 and Eq. 2 (e.g. $\lambda_p, F, Kn, \theta_a, \theta_z$) may have different influence on the relationship between T_c and T_r . The approach to evaluate how influential such variables and parameters are, is explained in Sect. 2.4. Finally, the relationships in Eq.1 and Eq.2 were determined and evaluated as described in Sect. 2.5.and 2.6.

2.2 Overview of the TUF-3D model

TUF-3D is a micro-scale urban energy balance model that represents the three-dimensional (3D) energy exchange in response to meteorological forcing, i.e. solar irradiance, wind speed and air temperature. The energy fluxes and (sub-) facet surface temperatures calculated with this model have been validated with measurements (Krayenhoff and Voogt, 2007). TUF-3D has also been used to estimate UST of heterogeneous pixels from the facet surface temperatures (Krayenhoff and Voogt, 2016), as well as to evaluate radiation models (Krayenhoff et al., 2014). TUF-3D describes sensible heat transfer in a simplified way by assuming that a constant flux layer extends to the surface, wherein the vertical profiles of wind speed and temperature are logarithmic (Krayenhoff and Voogt, 2007). This assumption can reduce computational costs in view of modeling large neighborhood or entire cities. In reality, heat transfer is complex because of the coherent turbulent structures and the complexity of the urban canopy layer due to the complex urban morphology and heterogeneous urban facets(Grimmond et al., 2011; Grimmond et al., 2010; Wang et al., 2014).The hypothesis of logarithmic vertical profiles of wind speed and air

temperature is widely adopted in urban micro-climate models, e.g. LASER/F (LATent, SEnsible, Radiation Fluxes) (Kastendeuch and Najjar, 2009; Kastendeuch et al., 2017). Lee et al. (2013) applied LASER/F to generate synthetic, high-resolution thermal images of building facets and evaluated the impact of the simplified description of momentum and heat transfer in LASEF/F by comparing it with a Computational Fluid Dynamics (CFD) model. The results showed that the impact on facet energy balance and surface temperature was relatively small. Accordingly, we accepted the hypothesis of logarithmic profiles in the urban canopy layer in TUF-3D.

2.3 Design of numerical experiments

Urban geometric parameters, including building planar area index (λ_p) and aspect ratio, and local meteorological conditions, including wind speed and solar radiation, have a direct impact on the relationship between T_c and T_r . To study the influence of these variables and parameters on the difference between T_c and T_r , several numerical experiments for different values of λ_p and aspect ratio under different meteorological conditions were carried out. The total number of numerical experiments is limited by available computational resources, so we limited the number of levels applied for each variable and parameter. According to Stewart et al. (2014), λ_p ranges from 0.1 to 0.90 and aspect ratio ranges between 0.1 and more than 2.5 for typical urban local climate zones. The λ_p ranges from 0.1 to 0.70 in this study because of the computing ability. Aspect ratio is calculated as the ratio of building height to street width. In TUF-3D, λ_p and ratio of building height to length (H/L) can be used to replace the

aspect ratio. In the TUF-3D, a building has a square horizontal section. The building length is equal to the building width of the building roof or base. The meteorological data, including solar radiation, wind speed, air temperature, air pressure, on cloudless days of each month from the Hong Kong Observatory were selected as input (Table 1).

Table 1. Surface building geometries and dates of meteorological parameters used in TUF-3D

λ_p	H/L	Dates of meteorological parameters (solar radiation, wind speed, air temperature, air pressure)
0.1-0.7	0.5-5.5	Feb 27 2010, Mar 10 2010, Apr 11 2010, May 25 2010, Jul 1 2010, Aug 2 2010, Sept 17 2010, Oct 28 2010, Nov 27 2010, Dec 7 2010

The values of thermal and radiative parameters of urban materials adopted in this study were also based on Stewart et al. (2014) and explore a broad range of conditions, so that the results of the analysis apply to a range of different urban conditions, e.g. from high-rise compacted city to open low-rise city space. The material properties in real world are complex, the values used in this study can represent the typical condition of the real world (Stewart et al., 2014). The material emissivity spectra of rooftop, wall facet and road were applied to estimate the emissivities in the Landsat 5 TM and ASTER spectral bands (Table 2). The material emissivity is calculated from the urban material spectral library (Kotthaus et al., 2014) and the satellite spectral response functions used in this study. We assume that roof is

295 constructed by concrete and brick, and the material emissivity of roof is the average
296 value of concrete and brick. The road is constructed by the concrete and asphalt and
297 the material emissivity of road is the average value of concrete and asphalt.

298 The geometric and meteorological parameters in Table 1 were combined with thermal
299 and radiative material properties in Table 2 to carry out the numerical experiments
300 with TUF 3D. In total about 17000 sets of data were carried out. Subsets of the results
301 were used in the sensitivity analysis described in Sect. 2.4, while the results of all
302 experiments were combined to determine our simple model (Sect. 2.5).

303

304

Table 2. Thermal and radiative properties used in TUF-3D (Stewart et al., 2014)

Surface properties	Group 1	Group 2	Group 3	Group 4	Group 5	Group 6	Group 7	Group 8	Group 9	10
Emissivity:										
roof	0.937	0.945	0.937	0.945	0.937	0.945	0.937	0.945	0.937	0.945
wall	0.956	0.886	0.956	0.886	0.956	0.886	0.956	0.886	0.956	0.886
ground	0.956	0.948	0.956	0.948	0.956	0.948	0.956	0.948	0.956	0.948
Albedo:										
roof	0.13	0.18	0.15	0.13	0.13	0.13	0.13	0.18	0.13	0.1
wall	0.25	0.2	0.2	0.25	0.25	0.2	0.2	0.25	0.25	0.2
ground	0.15	0.16	0.18	0.2	0.2	0.24	0.24	0.17	0.23	0.21
thermal conductivity(W/m/K) :										
roof	1.4									
wall	1.12									
ground	0.84									
volumetric heat capacity (10 ⁶ J/m3/K):										
roof	1.61	1.61	1.02	1.60	1.60	1.02	2.85	1.60	1.03	2.85
wall	1.75	3.57	2.28	2.58	2.58	2.28	0.32	2.01	2.29	2.01
ground	1.59	1.45	1.33	1.17	1.10	1.04	0.84	1.42	0.89	1.08

2.4 Evaluation of influential urban properties

Synthetic data on T_c and T_r were generated with TUF-3D and used as pseudo-observations to construct relationships between T_c and T_r (see Sect.2.5). Prior to that, we have evaluated the influence of urban properties on the relation between T_c and T_r as described in this Section.

The urban geometric parameters, λ_p and F , were used to represent the urban geometric characteristics and further study the relationship between T_r and T_c . The wind speed (w) in TUF-3D is set at above canopy height, estimated as twice the building height. Wind has different effects on roof and ground surface temperature and these effects depend on building density and aspect ratio (Nazarian and Kleissl, 2015). Daytime T_c can be written as a function of T_r , urban geometry, solar irradiance and solar position. The sensitivity of T_c to urban variables and parameters was evaluated by determining several different regressions, as listed in Table 3. The sensitivity analysis in Table 3 determines how the different variables affect the difference between T_c and T_r and which kind of equations should be constructed to estimate T_c .

Table 3 Sensitivity analysis of Eq.1. (the column of “specific sensitivity” describes each component of the sensitivity analysis by listing first the independent variables, then the variables taken as dependent; the column of “variables” lists the variables involved in the component sensitivity analysis; the column of “purposes” explains the objective of each component sensitivity analysis).

Specific sensitivity	Variables	Purposes
$T_c - T_r$ to λ_p	T_c, T_r, λ_p	How λ_p affects the difference T_c and T_r and what kind of relationship

		exists between T_c and λ_p
$T_c - T_r$ to F	T_c, T_r, F	How F affects the difference between T_c and T_r and what kind of relationship exists between T_c and F
$T_c - T_r$ to Kn, θ_a, θ_z	$T_c, T_r, Kn, \theta_a, \theta_z$	How solar parameters affect the difference between T_c and T_r and what kind of relationship exists between T_c and solar parameters
$T_c - T_r$ to wind speed (w)	T_c, T_r, w	How wind speed affects the T_c and T_r and what kind of relationship exists between T_c and wind speed
$T_c - T_r$ to material variations	T_c, T_r , material properties in Table 2	How different material properties affect the difference between T_c and T_r

2.5 Evaluation of the relationship between T_c and T_r

Determination of the relationship between T_c and T_r . The relative weight of variables and parameters is evaluated by the sensitivity analysis described in Sect.2.4, which also indicates which kind of relationship, e.g. linear, exists between $T_c - T_r$ and urban geometry parameters and climate variables. This can explain how urban geometry parameters and climate variables affect the difference between T_c and T_r and help to determine which kind of relationship between T_c and geometric/climate variables can be constructed. In Sect.2.4, the sensitivity analysis shows which parameters and variables are influential on T_c and which kind of relationship exists between T_c and these parameters.

In this section, the modelled T_c and T_r from TUF-3D were used to determine the relationship between T_c and T_r . According to the sensitivity analysis in Sect. 2.4, we included the following variables, $\lambda_p, F, Kn, \theta_a, \theta_z$, in the relationship to estimate T_c

from T_r in daytime (Eq.5) and included variables λ_p and F in the relationship to estimate T_c from T_r in nighttime (Eq.6). The relation between F and T_c is logarithmic according to the sensitivity analysis in Sect 2.4. The relationships between other variables and T_c are linear. About 6700 sets of T_c and T_r modelled by TUF-3D were used to regress the coefficients of Eq. 5 to estimate T_c from T_r in daytime. About 6500 sets of T_c and T_r modelled by TUF-3D under different structure and meteorological conditions in nighttime were used to regress the coefficients of Eq.6 to estimate T_c from T_r for the nighttime case. In both cases, the relationships are generic, in the sense that they apply to all cases explored by the numerical experiments. The accuracy of such parameterization of T_c is likely to increase when more predictive variables are applied. Since the sensitivity analysis suggests that a linear regression is sufficiently accurate, we determined the daytime parameterization of T_c as a multi-linear polynomial of the form:

$$T_c = a_1 * T_r + a_2 * \lambda_p + a_3 * \ln F + a_4 * K_n + a_5 * \theta_a + a_6 * \theta_z + a_0 \quad (5)$$

and nighttime:

$$T_c = b_1 * T_r + b_2 * \lambda_p + b_3 * \ln(F) + b_0 \quad (6)$$

$a_0 \sim a_6$ and $b_0 \sim b_3$ are regressed coefficients based on the numerical experiments under the conditions of urban geometries and atmospheric forcing listed in Table 1 which can cover most conditions of urban geometric parameters and climate conditions. Thus, the Eqs. 5 and 6 apply to a broad range of urban and weather conditions.

Validation of the relationship between T_c and T_r . The high-spatial-resolution airborne thermal images with 0.5 m spatial resolution were used to extract the component

temperatures such as temperatures of wall facets, rooftops, and roads. These images were observed at 12:40 pm on Aug 5, 2013 and 11:30 am on Oct 24, 2017. The building GIS data including building shape and height and Digital Surface Model (DSM) data were used to calculate the λ_p and F in order to estimate T_c and T_r from satellite data, while the high resolution airborne thermal camera data were applied to determine the component temperatures for each urban facet. For the high-resolution images, we obtained the mean component temperatures from different view images. The airborne thermal camera has a large FOV, so wall information can be acquired from the images. Then, T_r was estimated by the nadir high-spatial-resolution airborne thermal images and used to estimate the T_c based on the relationships constructed as described in this Section 2.5 (Eq.5). The T_c estimated from component temperatures and λ_p and F (Eq. 3) was used to validate the complete surface temperature estimated from T_r and the relationships described in this section.

2.6 Estimation of T_c from T_r

We have demonstrated how the relationship in Eq.5 and Eq.6 can be applied to actual satellite images. Here we describe briefly the procedure applied, while the results are presented in Sect.4.4

Daytime thermal images acquired by Landsat TM in 2010 were used to retrieve daytime T_r and ASTER nighttime thermal images acquired from Mar 13, 2013 and Aug 4, 2013 were used to retrieve T_r at night. The T_c images were then estimated by applying the relationships in Section 2.5 Eqs. (5) and (6).

381 The single channel method for T_r retrieval was used in this study (Li et al, 2013). For
 382 Landsat TM data, the effective transmittance of the atmosphere in band 6 of Landsat 5,
 383 i.e. the upward and downward atmospheric thermal radiance can be estimated using the
 384 NASA Atmospheric Correction Parameter Calculator (<http://atmcorr.gsfc.nasa.gov/>) to
 385 obtain channel radiance observed at the top of the urban canopy. The band 13 radiance of
 386 ASTER AST 09T product is the ground-leaving in-band radiance including the emission
 387 of surface and the reflected radiance by the surface, and the sky thermal irradiance in
 388 band 13 of the ASTER AST 09T product was used to calculate the downwelling radiance
 389 for the UST retrieval (Sobrino et al, 2007). The radiance leaving urban canopy can be
 390 written as:

$$391 \quad E(i) = \varepsilon(i)B(T_r(i)) + (1 - \varepsilon(i))R_{at}^{\downarrow}(i) \quad (7)$$

392 In the Equation (7), $\varepsilon(i)$ is the material emissivity of pixel i , calculated from the
 393 landcover and building GIS data as Yang et al. (2016) (see Sect. 3.3). $B(T_r(i))$ is the
 394 upwelling radiance of pixel i with radiometric temperature $T_r(i)$. $R_{at}^{\downarrow}(i)$ is the
 395 atmospheric downward radiance. When the effects of topography and geometric
 396 characteristics are considered, the thermal infrared ground-leaving radiance $E(i)$
 397 comprises the emittance of facets in the observed built-up space, the reflected radiance by
 398 the facets within pixel i and that by the neighbouring scene elements.

399 The radiometric temperatures were first retrieved with Landsat TM and ASTER data,
 400 then the complete surface temperature was calculated using the retrieved radiometric
 401 temperature (Eqs. 5 and 6). The urban geometric data and land use data were used to
 402 estimate the urban emissivity for the radiometric temperature. The building dataset and

Digital Surface Model (DSM) were also used to calculate λ_p and F . The seasonal effects on T_c were analyzed using the Landsat TM and ASTER data.

3. Study area and Data

3.1 Study area

Urban districts of Kowloon peninsula and Hong Kong Island across Hong Kong were selected as our study area (Figure 1). In brief, Hong Kong is a coastal city in South China (22° 17' N, 114° 09' E), and this study area has been recognized as a compact city with high-density living (Chen et al., 2012). Specifically, urban districts of Kowloon peninsula and Hong Kong Island is highly urbanized with mixed land use and high population density (Peng et al., 2017). Historical development of these urbanized areas has also resulted in commercial areas with high-density high-rise built environment for decades (Peng et al., 2017). Nowadays, there are even two high-rise buildings with more than 400m across the study area (the International Finance Centre and International Commerce Centre). Due to this high-rise, high-density urban environment, urban canyons have formed to influence microclimate significantly (Chen et al., 2012). In this condition, the remote sensing observation is also limited to part of urban facets. The observed radiometric surface temperature cannot represent the real urban surface temperature in such compacted city. Thus, the estimation of T_c is crucially important for urban climate research in Hong Kong, as a high quality thermal dataset should enhance the estimation of microclimate across a compact environment in a three-dimensional context.

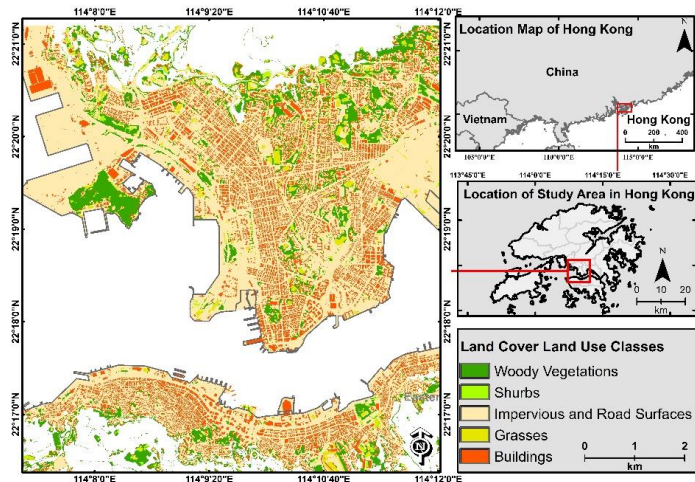
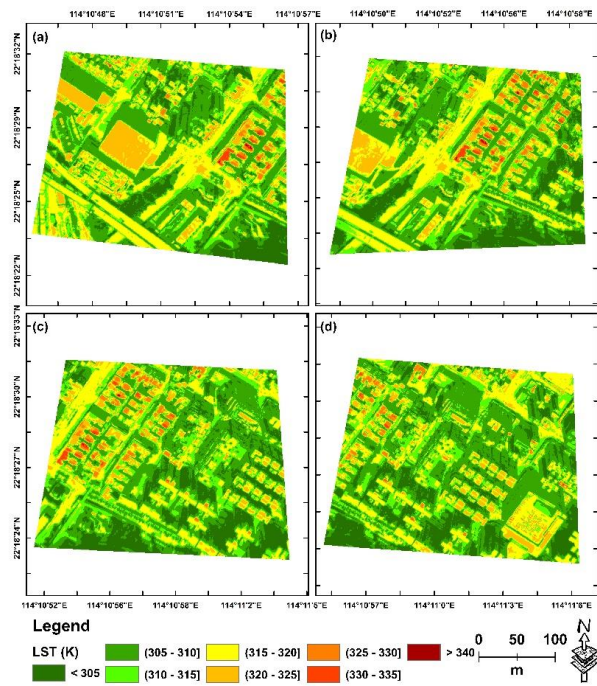


Figure 1. Study area: land uses in Kowloon peninsula and the Hong Kong Island

3.2 Thermal Remote sensing data

Landsat TM and ASTER data were used to estimate T_c in Hong Kong. The high spatial resolution thermal image data (Figure 2) captured on Aug 5 2013 and Oct 24 2017 were used in this study for validation. These images are observed at the nadir of the central image line. but the FOV of airborne thermal camera is large, so the images overlap, i.e. in different images there is the LST of the same target at different view angles. The estimated complete surface temperature was validated using the component temperatures (wall facets, rooftop and road) captured by the high resolution airborne thermal images and building data (Figure 2a to d). Additionally, the building data and Digital Surface Model (DSM) data at 1 m spatial resolution were used to calculate λ_p and F to estimate the complete surface temperature. More information about building data and LiDAR data can be found in Yang et al. (2016). The data acquired by satellite and

438 airborne platforms used in this study are listed in Table 4.



440 Figure 2. High spatial resolution thermal images acquired on Aug 5, 2013.

441 Table 4. Overview of satellite and airborne Thermal InfraRed (TIR) images used in this
442 study.

Data	Date	Local Time	Resolution(m)	Purpose
Landsat TM Band 6	Jan 14 2010	10:37 am	30 (resampled)	Retrieve T_r and T_c
	Mar 26 2010	10:43 am		
	Sept 18 2010	10:42 am		
	Oct 29 2010	10:36 am		
	Nov 11 2010	10:36 am		
	Dec 23 2010	10:42 am		

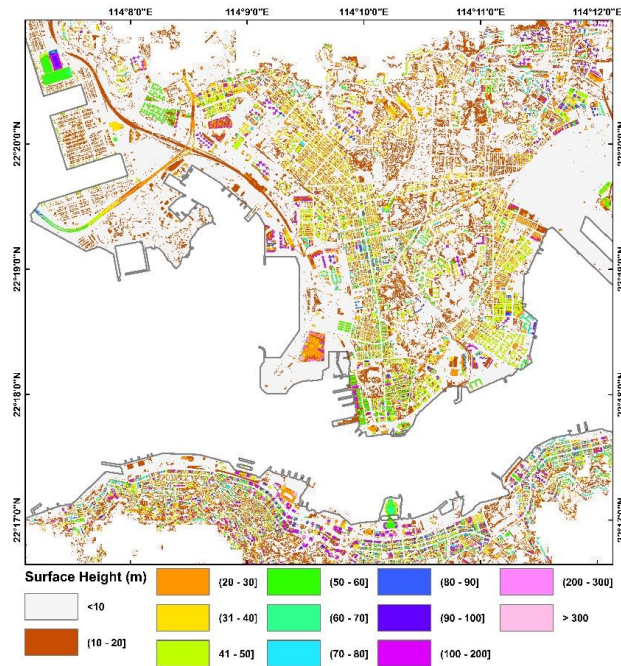
ASTER band 13	Mar 13 2013	10:36 pm	90	
	Aug 4 2013	10:36 pm		
Thermal images from thermal camera (FLIR T650sc) on airborne helicopter (500m)	Aug 5 2013	12:40 pm	0.5	Validation
	Oct 24 2017	11:30 am		

3.3 Land use and building information

We used airborne LiDAR data with 1 m spatial resolution and the building GIS data provided by the Hong Kong Civil Engineering and Development Department and Hong Kong Lands Department (Lai et al., 2012) (Figure 1). The LiDAR data were collected in December 2010 and January 2011 and used to determine and map the building heights (Figure 3). Land use data provided by the Hong Kong Planning Department and the 2010 building GIS data were used to estimate and map the material emissivity of Hong Kong (Figure 1). The overall classification accuracy of the land – use data in urban areas was 96% (according to the Hong Kong Planning Department). The land use classification data provide land cover information, e.g. tree, grassland and impervious surface with a spatial resolution of 6 m. Building GIS data were used to distinguish the impervious surface in buildings and road pavements (Figure 1). More information about emissivity estimation can be referred to Yang et al (2016).

The building GIS data and building heights (Figure 3) were used to calculate λ_p and F .

457 The λ_p with building data was calculated as the ratio of the building roof area to the area
 458 of a pixel, i.e. 30 m x 30 m for Landsat or 90 m x 90 m for ASTER. F was calculated as
 459 the ratio of the building wall area to the area of a pixel.



460

461 Figure 3. Building heights of Kowloon peninsula and the Hong Kong Island.

462 3.4. Ground-level meteorological data

463 The meteorological data used in this study (Table 5) were collected at the weather
 464 station located at the headquarters of the Hong Kong Observatory. Observations used in
 465 the experiments were limited to the time period between 0 am to 24 pm local time of
 466 sunny days in each month of year 2010. These days were selected because of the
 467 cloudless conditions. The air temperature ranges from 5.2 to 32.7 °C. Wind speed ranges
 468 from 0.1 to 4.3 m/s since in Hong Kong there are many high-rise buildings which reduce

469 wind speed in the surface layer. The highest solar irradiance is 1013.89 W/m^2 at noon on
 470 July 1st 2010. These meteorological data can cover most subtropical and mid-latitude
 471 climate conditions. Extreme cold areas may need further study.

472 Table 5. Overview of the meteorological data used in this study.

Variable	Description (units)	Date	Duration (hourly)
Solar irradiance	W/m^2	Feb 27 2010, Mar 10 2010,	0~24
Wind speed	m s^{-1}	Apr 11 2010, May 25	
Air temperature	$^{\circ}\text{C}$	2010, Jul 1 2010, Aug 2	
Air pressure at ground surface	mb	2010, Sept 17 2010, Oct 28 2010, Nov 27 2010, Dec 7 2010	

473

474 4. Results

475 The results of the sensitivity analysis described in Sect. 2.3 are presented first (Sect. 4.1),
 476 followed (Sect. 4.2) by the determination of the simple model described in Sect. 2.4. The
 477 model is then evaluated against the high resolution TIR image data (Sect.4.3) and applied
 478 to actual Landsat TM and ASTER image data (Sect. 4.4).

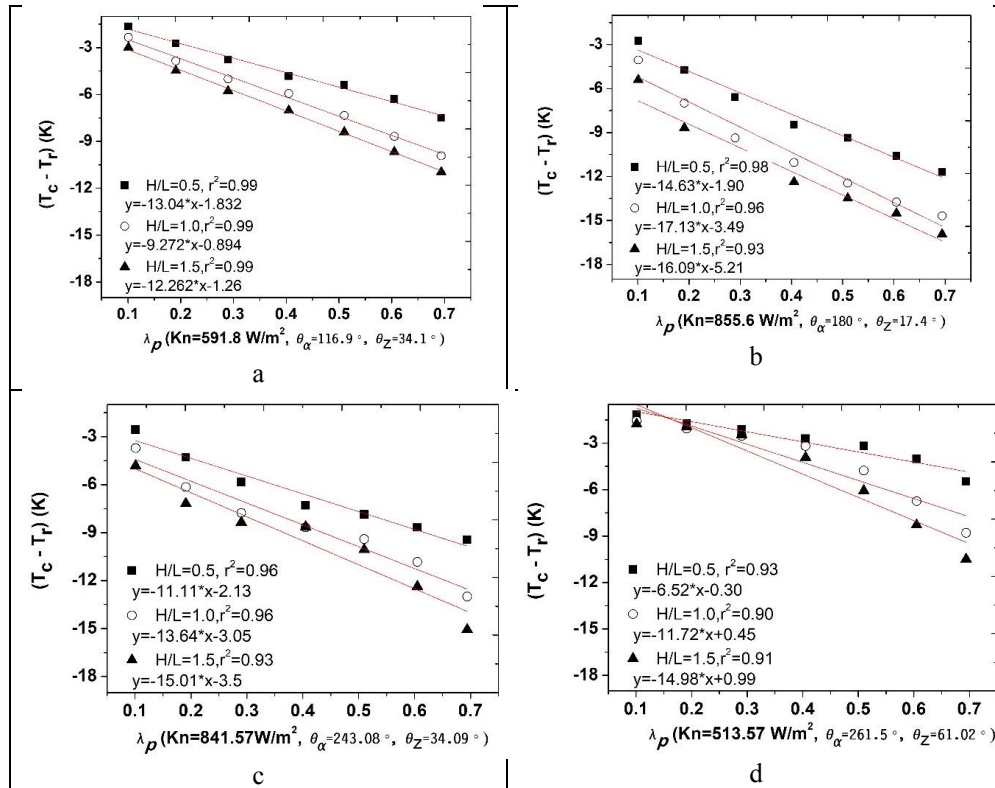
479 4.1 Sensitivity analysis of the relationship between T_c and T_r

480 4.1.1 Effects of λ_p on difference between T_c and T_r

481 A linear relationship between the difference ($T_c - T_r$) and λ_p was found for
 482 different solar and H/L daytime conditions (Figure 4). In Figure 4, the radiative and

483 thermal properties are set as Group 3 in Table 2. This experiment was performed at
484 constant values of H/L, wind speed, solar azimuth and zenith angles, i.e. changes in ($T_c -$
485 T_r) were due to changes in λ_p only. Overall, $T_c - T_r$ increased in magnitude (absolute
486 difference) with λ_p . With the increase of λ_p , the fraction of irradiance on street/road
487 facets decreases, while the fraction of irradiance on rooftop facets increases (Yang and Li,
488 2015). At the same time, the sensible heat flux at wall and street facets decreases with λ_p ,
489 while the sensible heat flux at roof facets remains nearly constant (Appendix Figure 1a).
490 The overall sensible heat flux decreases with λ_p due to the skimming effect (Grimmond
491 and Oke, 1999). During daytime, irradiance on street and wall facets decreases with
492 increasing λ_p because of the reduced sky view factor. Additionally, the proximity
493 between street and wall surfaces reduces sky view factors and increases drag on the
494 airflow reducing the convective heat transfer from the urban canopy to the surface layer
495 (Nazarian and Kleissl, 2015). The reduced irradiance leads to lower wall surface
496 temperature and sensible heat flux at wall facets. Note that the dominant factor
497 influencing canopy surface temperature during daytime is solar radiation. This makes the
498 wall and street surface temperature to decrease with increasing λ_p . Moreover, the
499 shading effect makes surface temperature of street and wall facets lower than roof facets.
500 With the increase of λ_p , a greater portion of the 3D facets cannot be observed by a nadir
501 viewing imaging radiometer. At the same time, T_c decreases with increasing λ_p due to the
502 decrease of wall and street surface temperatures (Appendix Figure 2). The change of T_r
503 with λ_p is not consistent and depends on the solar zenith angle and building H/L
504 (Appendix Figure 2) since both the solar angle and building H/L ratio determine
505 shadows. The difference between T_c and T_r changes with local solar time because of the

506 solar position and irradiance. At lower solar zenith angles (Figure 4b), the difference
 507 between T_c and T_r is larger than at higher solar zenith angles (Figure 4d). The linear
 508 dependence of $(T_c - T_r)$ on λ_p holds in all cases, but the slope changes with H/L and solar
 509 position, which should be taken into account in a generalized model. Street orientation
 510 also affects the irradiance and the shadow distribution and then affects both radiative and
 511 convective heat transfer. The material properties of roof, street and wall also affect the
 512 surface temperature distribution. This study did not consider the street orientation and
 513 material properties, which should be investigated in future work.



514 Figure 4. Relationships between the difference $(T_c - T_r)$ and λ_p under four different
 515 daytime solar conditions.

516 In these experiments, the decrease in wall facet temperature at night was generally
517 smaller than for rooftop temperature. One reason is the attenuation of radiation loss
518 because of radiative trapping in the urban canyons compared to rapid radiative cooling of
519 rooftops (Martilli et al., 2002). Overall, the sensible heat fluxes at roof facets and wall
520 facets are much smaller than in daytime. The sensible heat flux at roof facets is close to
521 zero and much smaller than the sensible heat flux at wall and street facets (Appendix
522 Figure 1). This is because the rooftop surface temperature is much lower than the wall
523 surface temperature at night (Nazarian and Kleissl, 2015). This thus induces a different
524 urban surface temperature distribution compared with daytime, and this difference is also
525 captured by the relationship between $(T_c - T_r)$ and λ_p at night (Figure 5). In addition,
526 radiative trapping increases with λ_p , thus $(T_c - T_r)$ at night increases with increasing λ_p .
527 With increasing λ_p , a larger rooftop fractional area is captured by a nadir viewing
528 imaging radiometer. The high-density of buildings can reduce the effectiveness of walls
529 in radiative and convective dissipation of excess energy, which results in higher wall
530 temperature than rooftops at night (Coutts et al., 2007). These make $(T_c - T_r)$ at night
531 increase with increasing λ_p . Higher λ_p implies a smaller sky view factor and results in
532 higher surface temperature within urban canyons. The cooling rate of wall and ground
533 facets is much smaller than that of roof facets, thus the temperature of the wall surface is
534 higher than rooftop, even in the early morning before sunrise (Kusaka and Kimura, 2004;
535 Nazarian and Kleissl, 2015). This results in nighttime T_r being lower than T_c . The
536 material properties also affect the cooling rate of urban surfaces, as described in a later
537 section.

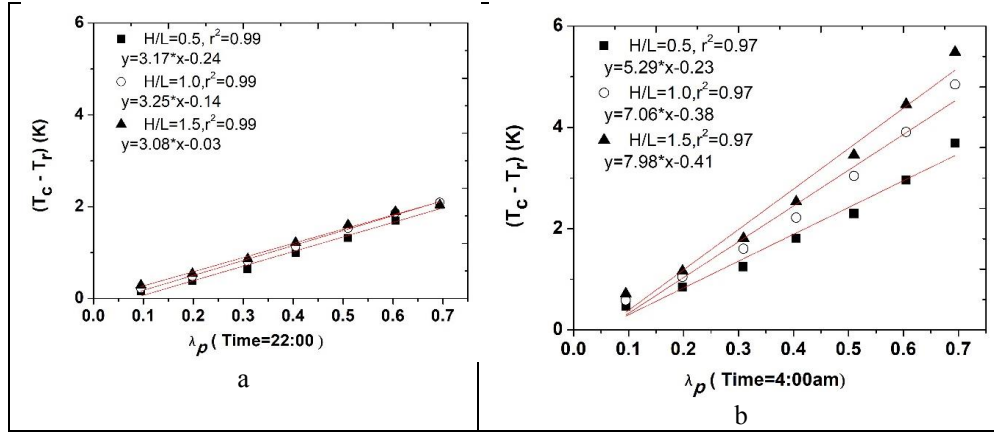


Figure 5. Relationship between the nighttime difference $(T_c - T_r)$ and λ_p .

4.1.2 Effects of F on the difference between T_c and T_r

When λ_p is constant, F and aspect ratio increase with H/L . During daytime, the relationship between $(T_c - T_r)$ and F is logarithmic when aspect ratio is smaller than 3.5 (Figure 6). When the aspect ratio and F increase, the street canyon becomes narrower and less solar radiation penetrates into the street canyon, thus irradiance onto street and wall facets decreases (Ali-Toudert and Mayer, 2006; Lemonsu et al., 2004; Nazarian and Kleissl, 2015) Yang and Li, 2015). The increase of aspect ratio contributes to the decrease of sensible heat flux at wall and ground facets (Nazarian and Kleissl, 2015). The total sensible heat flux increases with increasing aspect ratio, since the frontal area index and displacement height increase and, therefore, the aerodynamic resistance decreases. In daytime the energy loss by sensible heat exchange is mainly from rooftops (Martilli et al., 2002), while the irradiance onto rooftop facets does not vary since the λ_p does not change. Overall, these changes lead to a lower rooftop surface temperature. The difference between T_c and T_r increases gently with increasing F (Figures 6). The decrease

in irradiance is the dominant driver of wall and ground surface temperature, which still decreases notwithstanding the decrease in sensible heat flux with F . When the solar zenith angle θ_z is larger than 0, the wall and ground surface temperatures decrease less than when θ_z is equal to 0 (Figure 6d) and $T_c - T_r$ levels off when F is higher than a threshold F^* , which depends on irradiance and θ_z (Figure 6).

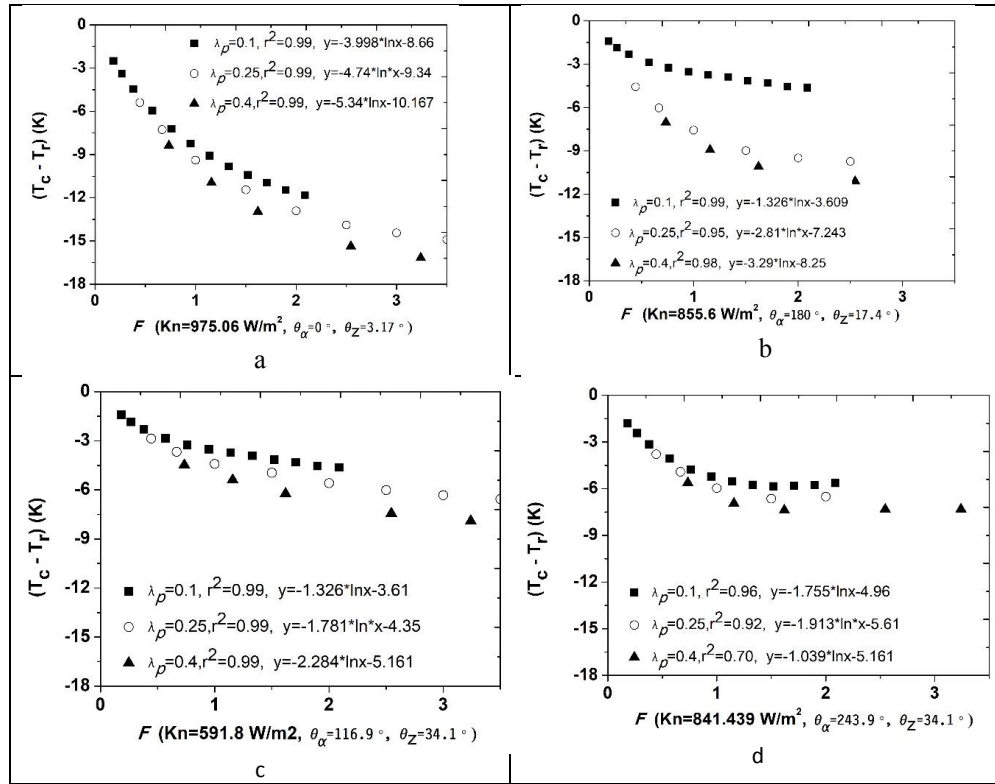


Figure 6. Relationship between the daytime difference $(T_c - T_r)$ and F under different solar conditions.

At night, $T_c - T_r$ increases with F at constant λ_p and then saturates (Figure 7). A higher aspect ratio reduces the sky view factor, longwave emittance and convective heat transfer to the atmospheric boundary layer. The sensible heat flux at wall and ground facets

decreases with increasing aspect ratio (Nazarian and Kleissl 2015). The cooling rate of wall and ground facet surfaces at night decreases with increasing aspect ratio, everything else being the same (Nazarian and Kleissl 2015). Road and wall facets are then cooling less than rooftop facets and also contributing to a road and wall facet temperature higher than rooftop facet temperature, resulting in an increase in $T_c - T_r$ with the aspect ratio. Convective heat exchange between wall facets and the atmospheric boundary layer increases with F , due to the effect of F on the temperature difference between the urban canyon and atmospheric boundary layer. This makes the wall surface temperature decrease, everything else being the same, and $T_c - T_r$ to level off past an initial increase with F (Figure 7). The difference between T_c and T_r increases with the 3D complexity of the observed urban target. It approaches zero with both F and λ_p approaching zero (i.e. for a flat target) and it is largest with $F = 4$ and $\lambda_p = 0.4$ in Figs. 6 and 7. A higher F -value at constant λ_p applies to taller buildings at constant areal (roof) density, while a higher λ_p at constant F applies to denser but lower buildings. In both cases an increase in either F or λ_p implies that more building facets cannot be observed by a nadir looking radiometer, thus explaining the increasing difference between T_c and T_r .

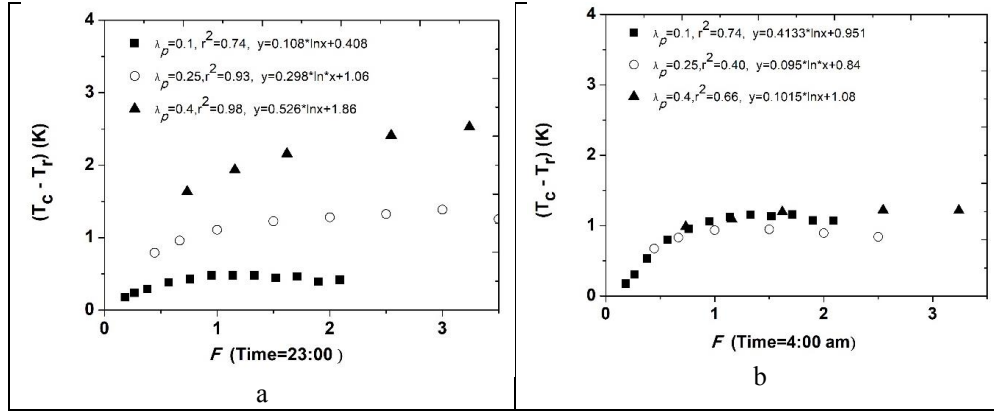
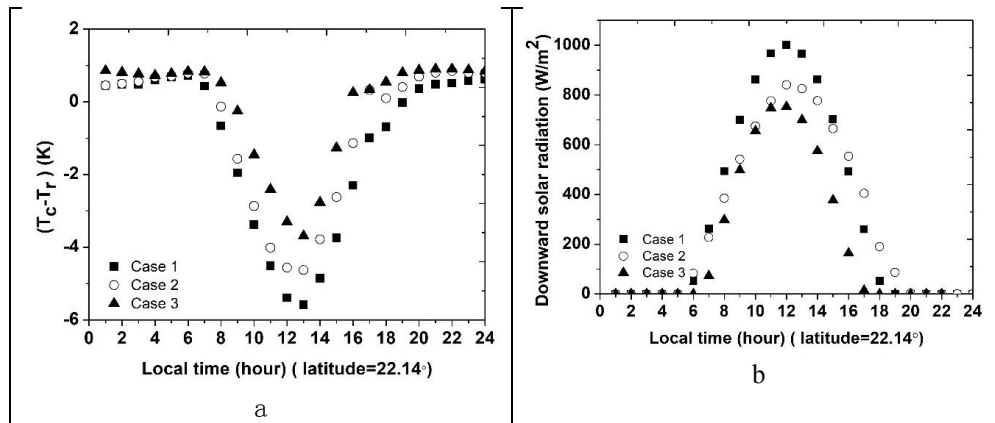


Figure 7. Relationship between the nighttime difference $(T_c - T_r)$ and F .

4.1.3 Effects of solar radiation on the difference between T_c and T_r

The irradiance onto urban surfaces changes with the solar angle, shading pattern and shortwave radiation intensity (Nazarian et al., 2017). The surface temperatures of road, rooftop and wall facets undergo a very different diurnal thermal cycle due to the solar position, urban geometry and material properties (Nazarian and Kleissl, 2015). This process contributes to the spatial variability of urban surface temperature and of turbulent heat transfer (Nazarian et al., 2018a; Nazarian et al., 2018b). Uneven irradiance caused by urban geometry and materials is the main driver of the spatial variability of daytime surface temperature under cloudless conditions, which results in the difference between T_c and T_r . The surface temperature of roads and wall facets is lower than roof temperature, due to the shadowing effect. The solar zenith angle and azimuth angle vary by the hour and day of year, which cast shadows at different locations within the urban canopy, thus determining the spatial variability of UST. Additionally, the magnitude of surface temperature heterogeneity changes with solar irradiance, e.g. surface temperature heterogeneity is higher in summer than in winter in Hong Kong. Figure 8 showed the

596 effects of solar irradiance and solar position on $(T_c - T_r)$ when $\lambda_p = 0.25$ and $H/L = 0.5$.
 597 This study used actual observations of solar irradiance on three days (Figure 8b). The
 598 results showed that when the irradiance is smaller, e.g. case 3 in Figure 8b, $(T_c - T_r)$ is
 599 smaller. When the irradiance increases, $(T_c - T_r)$ increases, since the rooftop temperature
 600 increases more than the wall temperature (Figure 10b, case 1 and case 2). The higher
 601 irradiance heats up the rooftop facets, which makes the T_r observed by remote sensors
 602 higher than T_c . The daytime solar radiation has little impact on the nighttime $T_c - T_r$ 3
 603 hours after sunset, e.g. 9:00 pm (Figure 8a).



604 Figure 8. Sensitivity of $T_c - T_r$ to irradiance: a) $T_c - T_r$ for cases 1 to 3 and; b) irradiance
 605 cases 1 to 3 as applied in a).

606 4.1.4 Effects of wind speed on the difference between T_c and T_r

607 TUF-3D is not originally designed for detailed assessments of the impacts of wind
 608 speed on surface temperature. This study adopted, however, a first-order evaluation of
 609 wind speed effects on $T_c - T_r$, assuming T_r to be observed at nadir. In our numerical
 610 experiments (see Sect. 2.2), wind speed at twice the building height was varied within the

range 1 to 6 m s⁻¹. The results show that $T_c - T_r$ decreases with increasing wind speed (Figure 9). This effect is particularly strong during daytime for a neighborhood with a large wall area, in which case directional shortwave irradiance generates a larger surface temperature heterogeneity which is modulated by wind speed. On average, our experiments give a sensitivity of $T_c - T_r$ to wind speed, with a 0.83 K reduction of $T_c - T_r$ per 1 m s⁻¹ increase in wind speed when $\lambda_p=0.2$ and H/L=2.5. These reductions of $T_c - T_r$ with wind speed vary with solar radiation and building density and height (Figure 9).

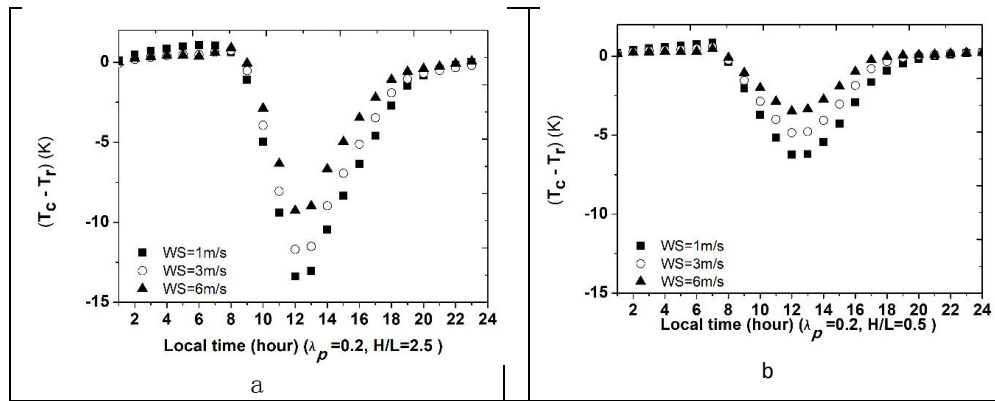
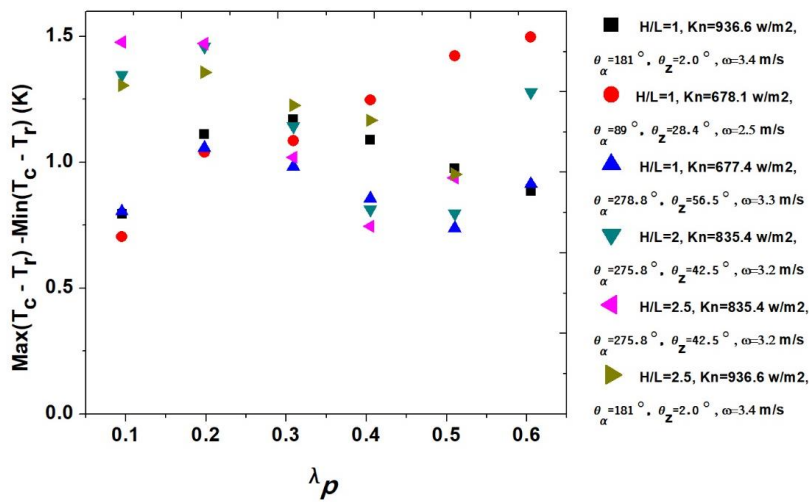


Figure 9. Sensitivity of $T_c - T_r$ to wind speed under different conditions: a, $\lambda_p=0.2$, H/L=2.5; b, $\lambda_p=0.2$, H/L=0.5.

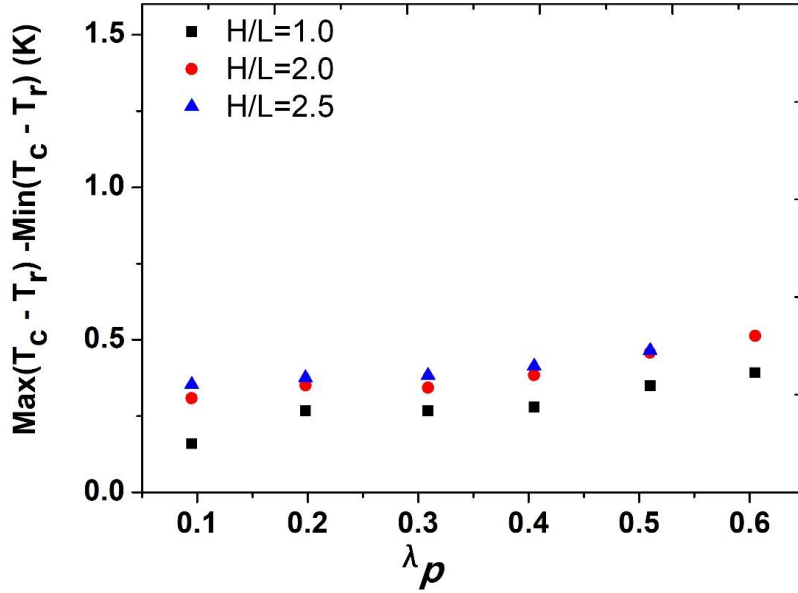
4.1.5 Sensitivity of $T_c - T_r$ to material properties

The material heterogeneity also causes thermal heterogeneity, but it is difficult to obtain exact information on materials in a city. Based on the material properties provided by (Stewart et al., 2014), the effects of material properties on $T_c - T_r$ were studied. Under different geometric and meteorological daytime conditions, the different materials can cause a 1.5 °C difference in $T_c - T_r$ (Figure 10). The differences in $T_c - T_r$ depend on the material distribution and solar position, although differences caused by material

627 properties remain much lower than $T_c - T_r$. We still recommend however, that the local
628 material properties should be used in numerical experiments to study the dependence of
629 $T_c - T_r$ on urban conditions. The impact of material properties on $T_c - T_r$ is smaller during
630 nighttime, i.e. less than 0.5 K and increasing with λ_p (Figure 11).



631
632 Figure 10. Impact of material properties on daytime $T_c - T_r$: ($\text{max}(T_c - T_r) - \text{min}(T_c - T_r)$)
633 obtained with the TUF – 3D numerical experiments and applying different combinations
634 of material properties in Table 2. (the parameter values applying to each experiment are
635 listed in the legend: H/L = ratio of building height to length; Kn = solar irradiance; θ_α =
636 sun azimuth angle; θ_z = sun zenith angle; ω = wind speed)



637

638 Figure 11. Impact of material properties on nighttime $T_c - T_r$: ($\max(T_c - T_r) - \min(T_c - T_r)$)
 639 obtained with the TUF – 3D numerical experiments and applying different combinations
 640 of material properties in Table 2. (the parameter values applying to each experiment are
 641 listed in the legend: H/L = ratio of building height to length)

642 4.2 Development of a simple empirical model to estimate $T_c - T_r$

643 The dependence of $T_c - T_r$ on geometric and climate variables and parameters has
 644 been explored in Sect 4.1. This analysis suggests that $T_c - T_r$ depends linearly on λ_p and
 645 the solar parameters (Kn , θ_a , θ_z), while the dependence on F is logarithmic.

646 Building upon these findings, a simple empirical model (see Eq. 5) to estimate T_c
 647 from T_r . f_d was constructed for daytime conditions by fitting Eq. 5 to the pseudo –
 648 observations generated by numerical experiments (Table 6). Two options were explored:
 649 a) by binning the pseudo – observations according to wind speed in steps of 1 ms^{-1} (see

650 first four cases in Table 6); b) by pooling the pseudo – observations for the entire range in
 651 wind – speed (Eq. 8). The RMSE increases with the wind speed (Table 6), but the RMSE
 652 for case (b) is still acceptable and not much larger than in three out of four (a) – cases,
 653 with $r^2 = 0.97$ for case (b). We can then conclude that a simple empirical model applies to
 654 a broad range of geometry and climate conditions and that it is not strictly needed to
 655 include wind–speed as a predictive variable. This is the empirical model we evaluated
 656 against high resolution airborne TIR images (Sect.4.3) and applied to satellite TIR
 657 (Sect.4.4).

658 Larger RMSEs were found when fitting the same model to pseudo – observations
 659 applying to sunrise (8 am) and sunset (5 pm), due to heat convection rather than solar
 660 irradiance being the main driver of UST at this time of the day (moreover with $T_c - T_r$
 661 being rather small). In contrast, the spatial variability in UST around noon, i.e. from
 662 11am to 3pm is driven by uneven irradiance associated with urban geometry.
 663 Accordingly, a smaller bias for estimated T_c , i.e. $\text{RMSE} < 1 \text{ K}$, was achieved by
 664 combining meteorological and urban geometry parameters. The numerical experiments
 665 suggest that the inclusion of urban geometry parameters is most significant in modelling
 666 T_c in the afternoon.

667 Table 6 Estimation of daytime T_c from T_r : regression relationships for different
 668 ranges in wind speed.

Wind speed (m/s)	Regression model	r^2	RMSE (K)
------------------------	------------------	-------	-------------

0~1	$T_c=1.065*T_r-2.883*\lambda_p-0.093*\ln(F)-0.021*Kn+0.014*\theta_a-0.088*\theta_z-10.509$	0.94	0.70
1~2	$T_c=0.930*T_r-6.757*\lambda_p-0.856*\ln(F)-0.006*Kn-0.003*\theta_a+0.053*\theta_z+20.003$	0.97	1.15
2~3	$T_c=0.927*T_r-6.509*\lambda_p-1.023*\ln(F)+0.003*Kn-0.020*\theta_a+0.181*\theta_z+14.384$	0.97	1.31
3~4	$T_c=0.773*T_r-3.712*\lambda_p-1.730*\ln(F)+0.004*Kn-0.001*\theta_a+0.139*\theta_z+59.377$	0.96	1.58

669

670 When the wind speed ranges from 0 to 6 m/s, the relationship to estimate T_c from T_r
671 at daytime can be written as:

672 $T_c=0.913*T_r-5.390*\lambda_p-1.090*\ln(F)+0.001*Kn-0.013*\theta_a+0.139*\theta_z+20.598$ (8)

673 Which gives $r^2=0.97$, RMSE=1.500 K. The plot of T_c simulated by TUF-3D and
674 estimated by Eq. 8 is presented in Figure 12a.

675 During nighttime, T_c-T_r levels off and it is rather small from 9 pm to 6 am (Figure 8),
676 while wind speed has a limited effect (Figure 9). Urban geometry still affects the energy
677 exchange and yields uneven cooling during nighttime, thus leading to the predictive
678 parameters to include in our simple empirical model (see Eq.6). Finally, the relationship
679 to estimate T_c from T_r at nighttime can be written as:

680 $T_c=0.927*T_r+3.455*\lambda_p+0.184*\ln(F)+21.320$ (9)

681 Which gives $r^2=0.98$, RMSE=0.690 K. The plot of T_c simulated by TUF-3D and
682 estimated by Eq. 9 is presented in Figure 12b.

When F is close to 0 and the surface is flat, T_c tends to T_r . The developed logarithmic function (see Eq. 8 and 9) would give undefined values in the limiting case $F = 0$. Even very small values of F , e.g. $F = 0.001$ and $\lambda_p = 0.1$, however, give a realistic value of 0.045 K for $T_c - T_r$ when applying Eq. 9 to a nearly flat surface with 280 K. To avoid any ambiguity, therefore, a threshold should be defined, e.g. $F > 0.001$, to constrain the range of validity of Eq. 8 and Eq. 9.

This empirical model was applied to estimate T_c from T_r retrieved from the ASTER nighttime data (see Sect.4.4).

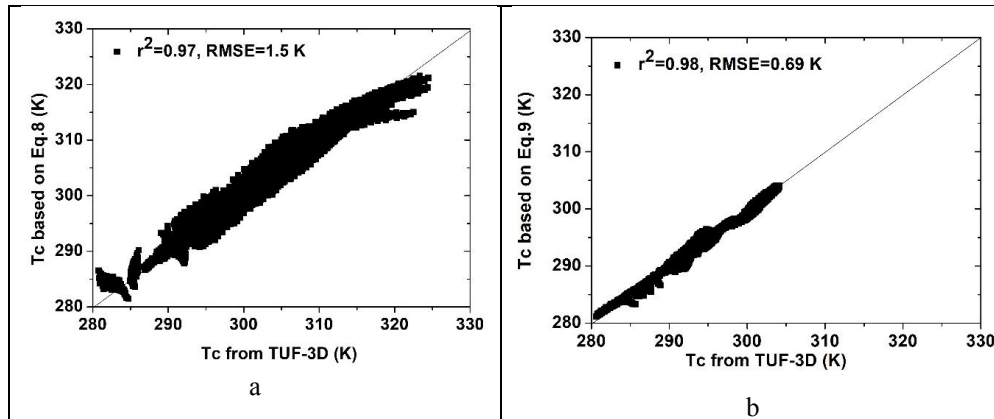


Figure 12. Scatter plot between actual and estimated T_c in the process of determining the coefficients: a, T_c from Eq. 8; b, T_c from Eq. 9.

4.3 Evaluation with high resolution airborne thermal data

Two experiments were conducted to evaluate our simple empirical model using high spatial resolution thermal infrared image data acquired on Oct 24, 2017 and Aug 5, 2013, where Oct 24, 2017 represents a day with lower solar irradiance (700 W/m^2) and Aug 5, 2013 was a day with higher irradiance (878.2 W/m^2). In addition, wind speed was rather

low and similar, i.e. 2 - 3 m s⁻¹ on both dates, so that we expected a larger thermal heterogeneity.

According to the methodology described above, we calculated the component temperatures within each 30 m x 30 m grid by averaging the 0.5 m x 0.5 m surface temperature for each surface type. Then we obtained the T_c from these component temperatures by Eq. 3. Then we estimated T_c from T_r by applying our Eq. 8 and evaluated our estimates against the T_c values obtained from the high resolution thermal images. We then compared these two sets of T_c (Figures 13a and 13b). We used the urban geometric parameters in our empirical relationships and the component temperatures derived from high-resolution images (Figure 2) at different view angles to determine the wall facet temperatures and the reference T_c . This validation gave reasonably accurate estimates of T_c , consistent with the expected accuracy of our empirical model (Eq. 8), with $r^2 = 0.75$ and RMSE = 1.09K on Aug 5, 2013 and $r^2 = 0.86$ and RMSE = 1.86K on Oct 24, 2017 (Figure 13b).

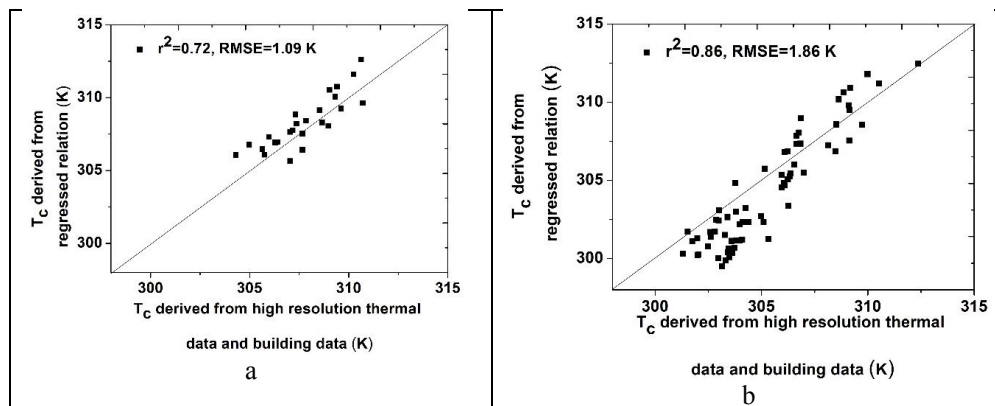


Figure 13. Comparison between T_c derived from T_r and T_c retrieved from component temperatures based on high resolution airborne thermal images: a, on Aug 5, 2013; b, Oct

24, 2017.

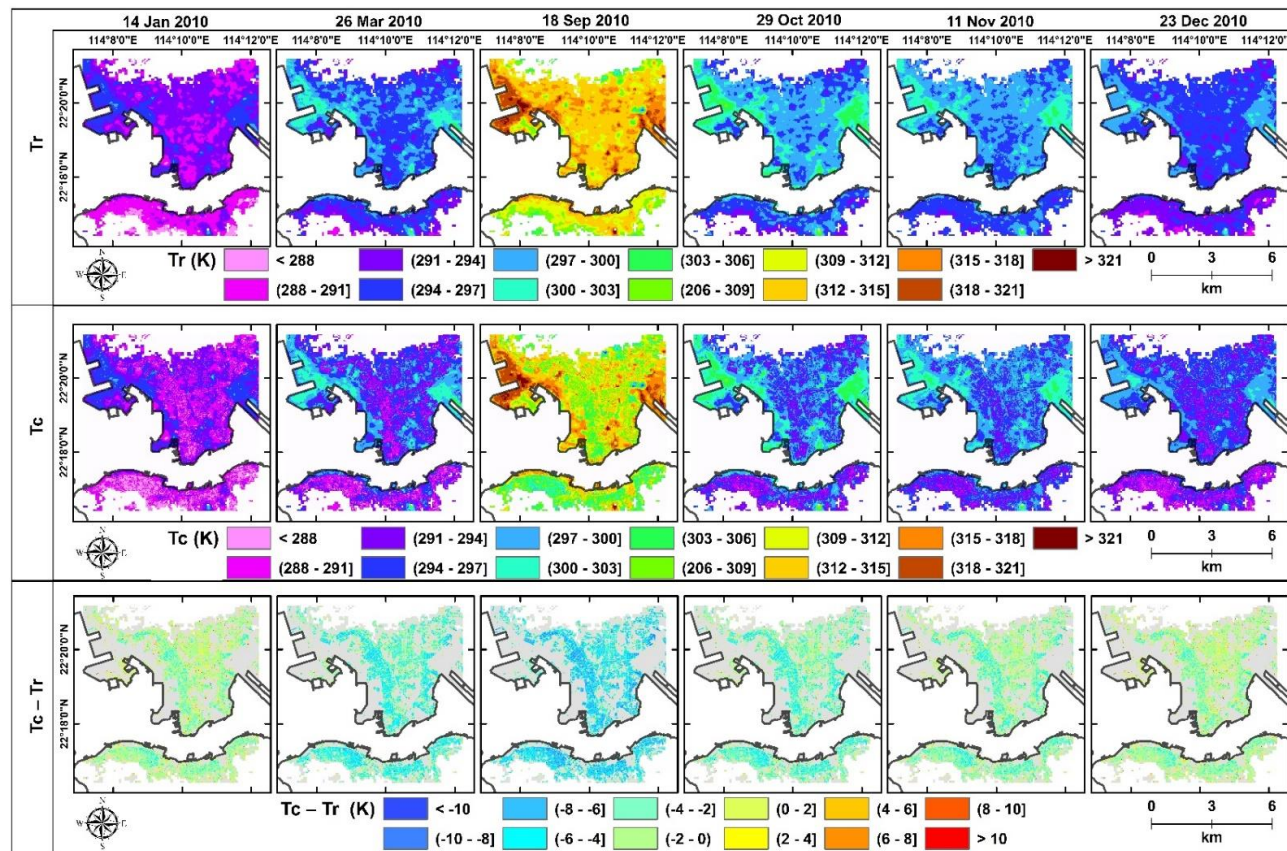
4.4 Complete urban surface temperature from satellite data

Finally, we estimated the daytime and nighttime complete urban surface temperature by applying our empirical models to Landsat TM and ASTER TIR image data respectively (Figures 14 and 15).

The previous sections and findings suggested that the procedure (Eq. 8) can be applied to an entire Landsat TM Band 6 image. The results showed that T_c over built-up areas was lower than over impervious areas and that during daytime, T_r was generally higher than T_c . The mean value of ($T_c - T_r$) was -2.15 K while in extreme cases it reached -6 K in built-up areas on Dec 23, 2010. $T_c - T_r$ has a strong seasonal trend associated with urban morphology and solar position (Table 7). For example, the mean value of $T_c - T_r$ on Sept 18, 2018, 2010 was -4.98K with extreme values as low as -10 K across built-up areas. This was possibly due to solar irradiance being the main driver of spatial variability of UST in daytime during the summer, when T_r is much higher than T_c , also taking into account the impact of shadows in the urban canyon, as determined by solar position. On the other hand, the solar elevation on Sept 18 2010 was much higher than on the other days (14 Jan 2010, 26 Mar 2010, Oct 29 2010, Nov 11 2010, Dec 23 2010), which determined the extreme ($T_c - T_r$) values. The higher solar elevation leads to rooftop temperatures higher than wall facet temperatures, since solar irradiance on the wall facets is lower. This result is also demonstrated by an increase in ($T_c - T_r$) when the solar elevation decreases and solar irradiance on the wall facets increases.

T_c was higher than T_r in several built-up areas during spring, autumn and winter,

736 while T_c was lower than T_r in almost all urban areas during summer. The mean absolute
737 value of $(T_c - T_r)$ was nearly equal to the absolute value of mean $(T_c - T_r)$ on Sept 8, 2010,
738 while the absolute value of mean $(T_c - T_r)$ on the other dates was much lower than the
739 mean absolute value (Table 7). This is possibly due to a lower T_r across several built-up
740 areas in non-summer seasons because of lower solar elevation angle, especially in the
741 areas with fewer high-rise buildings and lower density.



742

743 Figure 14. Radiometric, T_r , complete, T_c , surface temperature and their difference $T_c - T_r$, retrieved from Landsat TM Band 6 in 2010

744 based

on

Eq.8.

Table 7. Difference of $T_c - T_r$ between complete and radiometric urban surface temperature in entire images.

Date	Mean ($T_c - T_r$) (K)	Mean absolute value of ($T_c - T_r$) (K)
Jan 14 2010	-0.861	2.133
Mar 26 2010	-3.233	3.640
Sept 18 2010	-4.981	5.133
Oct 29 2010	-2.442	3.00
Nov 30 2010	-1.720	2.530
Dec 23 2010	-0.910	2.150
Mar 13 2013	0.310	0.784
Aug 4 2013	-0.230	0.680

The nighttime T_c was estimated by applying Eq. (9) with ASTER-TIR radiometric data and building data. The T_c was found to be higher than T_r over built-up areas, with the difference reaching 2 K (Figure 14). The Nighttime ($T_c - T_r$) was higher in spring than in summer, while the daytime ($T_c - T_r$) was lower in summer than in winter. Average and standard deviation of ($T_c - T_r$) during the summer nighttime (Aug 4, 2013) were -0.21K and 1.13K respectively, while average and standard deviation on a winter nighttime (Mar 13 2013) were 0.30 K and 1.13 K respectively.

Specifically, in a high-density built environment, T_c was higher than T_r at night of both Mar 13 and Aug 4 2013. Lower nighttime T_r then T_c can be explained by heat dissipation at rooftop facets being larger than at wall or street facets. This process of radiative and convective dissipation is different in daytime, which may result in a

lower rooftop surface temperature in the late evening. The latter is likely to determine the T_r observed by a nadir looking TIR imaging radiometer.

Another important factor is daytime heat storage and nighttime heat dissipation by wall facets. The solar elevation angle on Mar 13, 2013 was lower than on August 4 2013, thus solar irradiance on wall facets was higher in August, and it induced increasing heat storage at wall facets. In addition, building morphology can reduce both radiative and convective cooling of wall facets: wall facet temperature can be higher than rooftop temperature at night. Solar irradiance on wall facets is lower in summer daytime and rooftop temperature decreases rapidly after sunset. This increases the spatial variability of surface temperature during summer daytime, but reduces it during summer nighttime. Thus, the spatial variability of surface temperature at night in summer is smaller than in spring. T_c on August 4 2013 was lower than T_r in areas with lower building density. This is because the wall facet temperature is lower than the rooftop temperature in some areas at night. In winter, the solar radiation heats up more wall facets within the urban space because of the lower solar elevation angle than in summer. Thus, the wall facet temperature in winter is higher than rooftop temperature, while the wall facet temperature in summer is a little higher than the rooftop temperature.

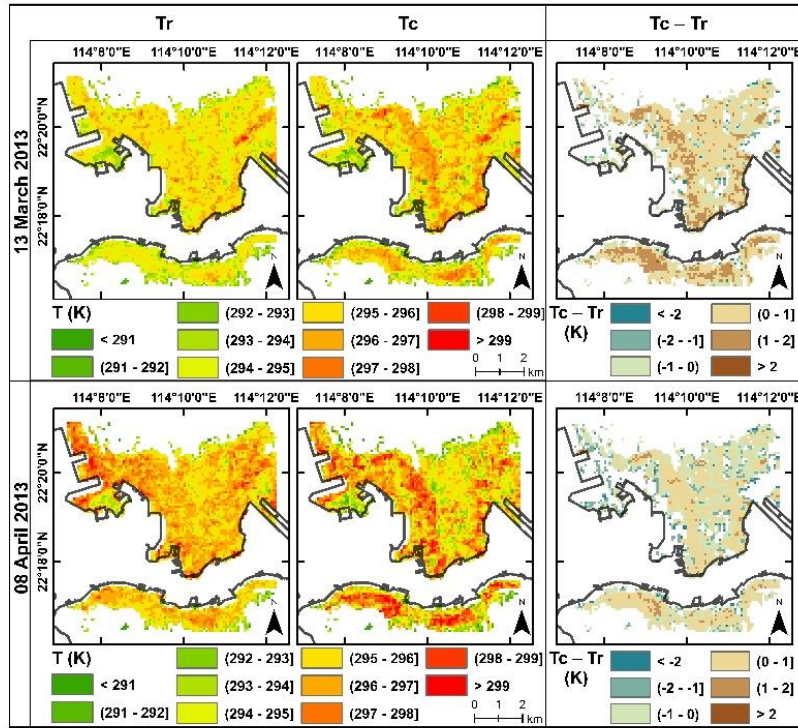


Figure 15. Nighttime T_r and T_c estimated by applying Eq.9 from ASTER image data and GIS building data in 2013.

5. Discussion

In this study, the TUF-3D model was used to derive synthetic data on urban climate under different and controlled conditions. The data from TUF-3D model were used to analyze the effects of different urban geometric and climate parameters on the relationship between T_c and T_r in daytime and nighttime. In addition, the numerical experiments showed that the geometric effects on the relationship between T_c and T_r are different at daytime and nighttime. It is difficult to obtain this information based on

observational data. This study demonstrates an operational method to estimate T_c from satellite TIR data. The method developed in this study has been validated using the thermal infrared image data at high spatial resolution. In principle, it would be ideal to acquire the high resolution TIR image data simultaneously with either the Landsat TM or ASTER acquisitions for evaluating the estimated T_c , but this was not feasible due to practical constraints on the airborne acquisitions. The accuracy of the retrieval of T_r with Landsat TM and ASTER radiometric data is well documented in the literature (Li et al., 2013; Gillespie et al., 1998).

Formatted: Underline, Highlight

This study only discussed the estimation of T_c from nadir viewed remote sensing thermal data. (Jiang et al., 2018) estimated T_c from airborne thermal data at different view angles and results showed that the observed radiometric temperature is closest to T_c when viewing azimuth and zenith angles are $\theta_a \pm 90^\circ$ and $\theta_z = 45 \sim 60^\circ$. For off-nadir images, the data can capture information on wall facets, and results show that the observed T_r at off-nadir angles is closer to T_c than the nadir data. (Jiang et al., 2018) also indicated that T_c can be improved by measuring directional radiometric temperatures. Currently the SENTINEL-3 SLSTR can provide two-angular thermal images at nadir and forward direction (about 53°), extending the data record collected by the (A)ATSR series instruments (<https://sentinel.esa.int/web/sentinel/technical-guides/sentinel-3-slstr/instrument>). This may provide an opportunity to estimate the complete surface temperature in the future, albeit at low spatial resolution.

It is difficult to obtain the exact material properties within the mixed pixels. Several studies have shown that geometry is the main determinant of the urban surface

temperature distribution (Krayenhoff and Voogt, 2016; Voogt and Oke, 2003), while the material properties still have impact on urban surface temperature distribution. In alternative, this study used the predefined material properties of urban surface models to better evaluate the relationships between T_c and T_r associated with urban materials. This approach may reduce the bias caused by material heterogeneity, while exact information on material properties within a pixel cannot be obtained from satellite images. Sensitivity tests also have been conducted using different typical material properties provided by (Stewart et al., 2014), and results showed that the different material properties caused less than 1.5 °C spread under different geometric and meteorological conditions. This proved that urban geometry has more effect on urban surface temperature distribution than materials. However, we still recommend that the local material properties should be used in further studies.

The TUF-3D can model the radiation and energy flux applying to simple building arrays. Therefore, the complexity of building shape and distributions in real-world, and its associated effects on surface temperature distribution have not been explored. The validation was also carried out over areas without vegetation. In addition, the actual building outlines and structures are not as uniform as in the TUF-3D model. Thus, the simple model developed in this study to estimate the complete urban surface temperature still needs more detailed validation e.g. with in-situ measurements with radiometers or IR-temperature sensor. The solar irradiance and position at a particular location vary across seasons. In this study, the latitude was set as 22.14°N. The relationships between T_r and T_c at different latitudes will be studied further.

We only considered the UST heterogeneity caused by buildings within a pixel, while

buildings in neighboring pixels may also influence the spatial variability of temperature by shadowing effect and interference on heat convection. In this study, the highest building is 415.8 m. The shadow of this building may affect adjacent pixels, especially at sunrise and sunset. Thus, our empirical models are more suitable for a city with lower fractional abundance of high-rise buildings.

In this study, the impacts of vegetation cover on temperature was excluded since Hong Kong is an extremely urbanized area. However, vegetation may have a strong effect in some cities with complex interactions, due to the shape and density of vegetation canopy and building morphology. In addition, evapotranspiration of vegetation cover can significantly reduce urban temperatures. Vegetation cover reduces the wind speed and sky view factor. Therefore, further applications using the empirical models developed in this study to other cities may need to require refinements by including the effects of vegetation.

Finally, wind direction was not included in the modelling. Although wind direction is important in urban energy exchange, it is mostly influencing areas with regular orientation of streets and identical city blocks. However, considering that orientation of streets is not regular across Hong Kong (Nichol and Wong, 2005), wind direction may not have a strong effect on UST. For future studies in a city with regularly oriented streets, integration with the relative angle between wind and street orientation may be essential.

6. Conclusion

This study explored the relationship between complete urban surface temperature and

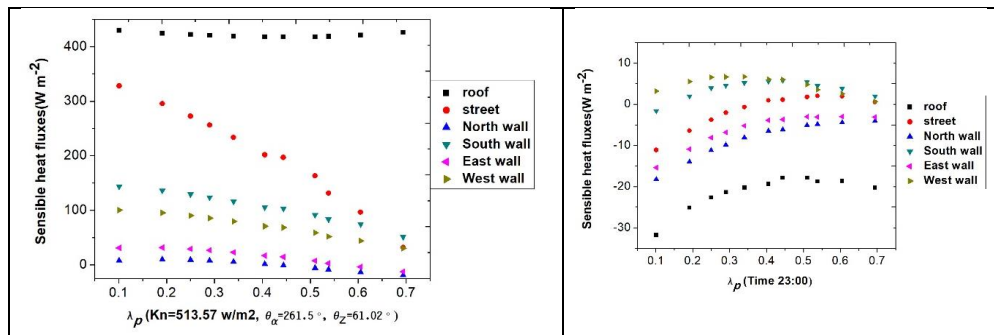
the nadir radiometric temperature observed from satellites. The relationships between urban geometry and difference between T_r and T_c were developed and results showed that the correlation coefficients are 0.97 for daytime and 0.98 for nighttime, and overall RMSEs are 1.5°C for daytime and 0.69°C for nighttime. Daytime relationships between T_r and T_c have been evaluated in this study using higher resolution airborne thermal images and results showed that the correlation coefficients and RMSEs are 0.72, 1.09°C on August 6, 2013 at 12:40 pm; and 0.86 and 1.86°C on October 24, 2017 at 11:30 am. The developed relationships were also used to estimate the complete surface temperature from satellite data in Hong Kong. The results showed that daytime difference between T_c and T_r can reach 10°C in summer and 6°C in winter, and the difference at night can reach to 2°C in spring and summer. This study provides a simplified method for estimating complete surface temperature from satellite data, and the multi-angular TIR radiometric data will be used to improve the estimation of urban complete surface temperature in the near future.

Acknowledgement

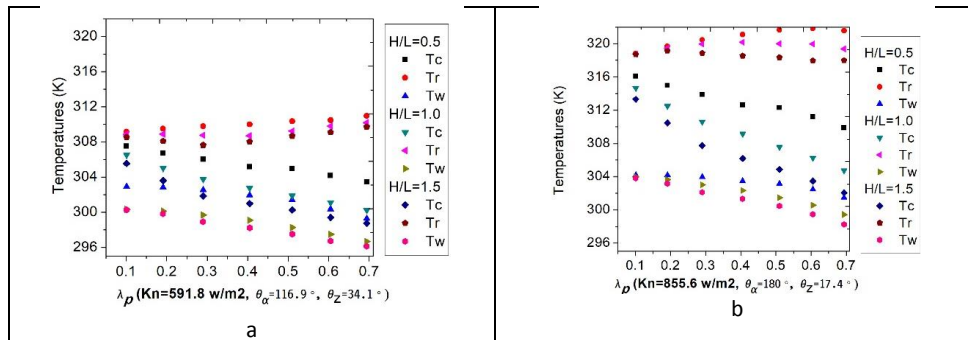
This work was supported in part by the grant of Early Career Scheme (project id: 25201614) from the Research Grants Council of Hong Kong, the grant 1-ZE24 from the Hong Kong Polytechnic University; and Grants by National Natural Science Foundation of China (41671430, 41901283, 41571366, 61976234, 61601522) and grant number 69-18ZX10347 by Guangzhou University. The authors thank the Hong Kong Planning Department, Hong Kong Lands Department, the Hong Kong Civil Engineering and Development Department, the Hong Kong Observatory and the Hong Kong Government Flying Service for the planning, building GIS, weather and climate, and airborne Lidar

877 data, and NASA LP DAAC for the Landsat and ASTER satellite imagery. Massimo
878 Menenti acknowledges the support of grant P10-TIC-6114 by the Junta de Andalucía and
879 the SAFEA Long-Term-Projects of the 1000 Talent Plan for High-Level Foreign Experts
880 (grant No. WQ20141100224).

881 Appendix



882
883 Figure 1 Change of sensible heat fluxes with λ_p : a daytime; b nighttime.



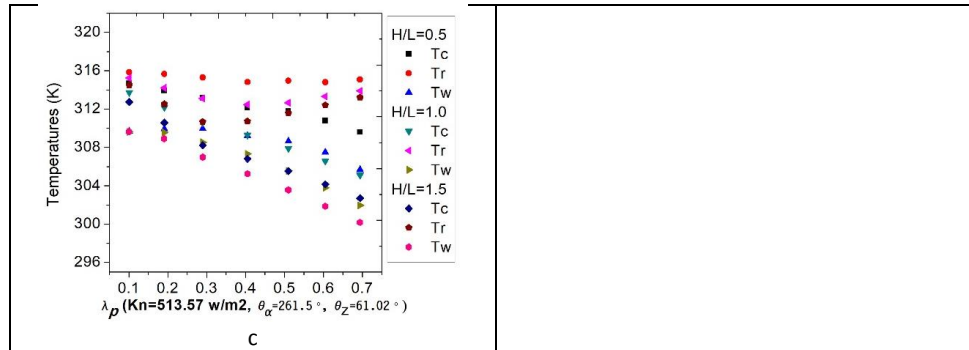


Figure 2. Change of T_r and T_c and T_w (wall surface temperature) with λ_p .

References:

- Adderley, C., Christen, A. and Voogt, J.A., 2015. The effect of radiometer placement and view on inferred directional and hemispheric radiometric temperatures of an urban canopy. *Atmos. Meas. Tech.*, 8(7): 2699-2714.
- Ali-Toudert, F. and Mayer, H., 2006. Numerical study on the effects of aspect ratio and orientation of an urban street canyon on outdoor thermal comfort in hot and dry climate. *Building and Environment*, 41(2): 94-108.
- Allen, M., Voogt, J. and Christen, A., 2018. Time-Continuous Hemispherical Urban Surface Temperatures. *Remote Sensing*, 10(1): 3.
- Arnfield, A.J., 2003. Two decades of urban climate research: a review of turbulence, exchanges of energy and water, and the urban heat island. *International Journal of Climatology*, 23(1): 1-26.
- Arnfield, A.J. and Grimmond, C., 1998. An urban canyon energy budget model and its application to urban storage heat flux modeling. *Energy and buildings*, 27(1): 61-68.
- Becker, F. and Li, Z.L., 1995. Surface temperature and emissivity at various scales: Definition, measurement and related problems. *Remote Sensing Reviews*, 12(3-4): 225-253.
- Chen, L. et al., 2012. Sky view factor analysis of street canyons and its implications for daytime intra-urban air temperature differentials in high-rise, high-density urban areas of Hong Kong: a GIS-based simulation approach. *International Journal of Climatology*, 32(1): 121-136.
- Cheng, J., Liang, S., Wang, J. and Li, X., 2010. A Stepwise Refining Algorithm of Temperature and Emissivity Separation for Hyperspectral Thermal Infrared Data. *IEEE Transactions on Geoscience and Remote Sensing*, 48(3): 1588-1597.
- Coutts, A.M., Beringer, J. and Tapper, N.J., 2007. Impact of Increasing Urban Density on Local Climate: Spatial and Temporal Variations in the Surface Energy Balance in

- Melbourne, Australia. *Journal of Applied Meteorology and Climatology*, 46(4): 477-493.
- Dousset, B. and Gourmelon, F., 2003. Satellite multi-sensor data analysis of urban surface temperatures and landcover. *ISPRS Journal of Photogrammetry and Remote Sensing*, 58(1-2): 43-54.
- Grimmond, C. et al., 2011. Initial results from Phase 2 of the international urban energy balance model comparison. *International journal of climatology*, 31(2): 244-272.
- Grimmond, C. et al., 2010. The international urban energy balance models comparison project: first results from phase 1. *Journal of applied meteorology and climatology*, 49(6): 1268-1292.
- Grimmond, C. and Oke, T.R., 1999. Aerodynamic properties of urban areas derived from analysis of surface form. *Journal of Applied Meteorology*, 38(9): 1262-1292.
- Gillespie, A. et al., 1998. A temperature and emissivity separation algorithm for Advanced Spaceborne Thermal Emission and Reflection Radiometer (ASTER) images. *Geoscience and Remote Sensing, IEEE Transactions on*, 36(4): 1113-1126.
- Jiang, L. et al., 2018. Remote estimation of complete urban surface temperature using only directional radiometric temperatures. *Building and Environment*, 135: 224-236.
- Kanda, M., Kanega, M., Kawai, T., Moriwaki, R. and Sugawara, H., 2007. Roughness Lengths for Momentum and Heat Derived from Outdoor Urban Scale Models. *Journal of Applied Meteorology and Climatology*, 46(7): 1067-1079.
- Kanda, M. et al., 2005. A simple energy balance model for regular building arrays. *Boundary-Layer Meteorology*, 116(3): 423-443.
- Kastendeuch, P.P. and Najjar, G., 2009. Simulation and validation of radiative transfers in urbanised areas. *Solar Energy*, 83(3): 333-341.
- Kastendeuch, P.P., Najjar, G. and Colin, J., 2017. Thermo-radiative simulation of an urban district with LASER/F. *Urban Climate*, 21: 43-65.
- Krayenhoff, E.S., Christen, A., Martilli, A. and Oke, T.R., 2014. A Multi-layer Radiation Model for Urban Neighbourhoods with Trees. *Boundary-Layer Meteorology*, 151(1): 139-178.
- Krayenhoff, E.S. and Voogt, J., 2007. A microscale three-dimensional urban energy balance model for studying surface temperatures. *Boundary-Layer Meteorology*, 123(3): 433-461.
- Krayenhoff, E.S. and Voogt, J.A., 2016. Daytime Thermal Anisotropy of Urban Neighbourhoods: Morphological Causation. *Remote Sensing*, 8(2): 108.
- Kusaka, H. and Kimura, F., 2004. Thermal Effects of Urban Canyon Structure on the Nocturnal Heat Island: Numerical Experiment Using a Mesoscale Model Coupled with an Urban Canopy Model. *Journal of Applied Meteorology*, 43(12): 1899-1910.
- Lai, A., So, A.C., Ng, S. and Jonas, D., 2012. The Territory-Wide Airborne Light Detection and Ranging Survey for the Hong Kong Special Administrative Region, The 33RD Asian Conference on Remote Sensing, pp. 26-30.
- Lee, D. et al., 2013. Modeling and observation of heat losses from buildings: The impact of geometric detail on 3D heat flux modeling.

961 Lemonsu, A., Grimmond, C.S.B. and Masson, V., 2004. Modeling the Surface Energy
 962 Balance of the Core of an Old Mediterranean City: Marseille. *Journal of Applied*
 963 *Meteorology*, 43(2): 312-327.
 964 Li, Z.-L. et al., 2013. Satellite-derived land surface temperature: Current status and
 965 perspectives. *Remote Sensing of Environment*, 131: 14-37.
 966 Martilli, A., Clappier, A. and Rotach, M.W., 2002. An Urban Surface Exchange
 967 Parameterisation for Mesoscale Models. *Boundary-Layer Meteorology*, 104(2):
 968 261-304.
 969 Morrison, W. et al., 2018. A novel method to obtain three-dimensional urban surface
 970 temperature from ground-based thermography. *Remote Sensing of Environment*,
 971 215: 268-283.
 972 Nazarian, N., Fan, J., Sin, T., Norford, L. and Kleissl, J., 2017. Predicting outdoor
 973 thermal comfort in urban environments: A 3D numerical model for standard
 974 effective temperature. *Urban Climate*, 20: 251-267.
 975 Nazarian, N. and Kleissl, J., 2015. CFD simulation of an idealized urban environment:
 976 Thermal effects of geometrical characteristics and surface materials. *Urban*
 977 *Climate*, 12(0): 141-159.
 978 Nazarian, N., Martilli, A. and Kleissl, J., 2018a. Impacts of Realistic Urban Heating, Part
 979 I: Spatial Variability of Mean Flow, Turbulent Exchange and Pollutant Dispersion.
 980 *Boundary-Layer Meteorology*, 166(3): 367-393.
 981 Nazarian, N., Martilli, A., Norford, L. and Kleissl, J., 2018b. Impacts of Realistic Urban
 982 Heating. Part II: Air Quality and City Breathability. *Boundary-Layer Meteorology*.
 983 Oke, T., 1988. The urban energy balance. *Progress in Physical geography*, 12(4): 471-508.
 984 Peng, F., Wong, M.S., Ho, H.C., Nichol, J. and Chan, P.W., 2017. Reconstruction of
 985 historical datasets for analyzing spatiotemporal influence of built environment on
 986 urban microclimates across a compact city. *Building and Environment*, 123: 649-
 987 660.
 988 Roth, M., Oke, T.R. and Emery, W.J., 1989. Satellite-derived urban heat islands from
 989 three coastal cities and the utilization of such data in urban climatology.
 990 *International Journal of Remote Sensing*, 10(11): 1699-1720.
 991 Stewart, I.D., Oke, T.R. and Kravtsov, E.S., 2014. Evaluation of the 'local climate
 992 zone' scheme using temperature observations and model simulations.
 993 *International Journal of Climatology*, 34(4): 1062-1080.
 994 Voogt, J.A. and Oke, T.R., 1997. Complete urban surface temperatures. *Journal of*
 995 *Applied Meteorology*, 36(9): 1117-1132.
 996 Voogt, J.A. and Oke, T.R., 2003. Thermal remote sensing of urban climates. *Remote*
 997 *sensing of environment*, 86(3): 370-384.
 998 Wang, L. et al., 2014. Turbulent Transport of Momentum and Scalars Above an Urban
 999 Canopy. *Boundary-Layer Meteorology*, 150(3): 485-511.
 1000 Weng, Q., 2009. Thermal infrared remote sensing for urban climate and environmental
 1001 studies: Methods, applications, and trends. *ISPRS Journal of Photogrammetry and*
 1002 *Remote Sensing*, 64(4): 335-344.
 1003 Yaghoobian, N., Kleissl, J. and Kravtsov, E.S., 2010. Modeling the Thermal Effects of
 1004 Artificial Turf on the Urban Environment. *Journal of Applied Meteorology and*
 1005 *Climatology*, 49(3): 332-345.

1006 Yang, J. et al., 2016. Development of an improved urban emissivity model based on sky
1007 view factor for retrieving effective emissivity and surface temperature over urban
1008 areas. *ISPRS Journal of Photogrammetry and Remote Sensing*, 122: 30-40.
1009 Yang, X. and Li, Y., 2015. The impact of building density and building height
1010 heterogeneity on average urban albedo and street surface temperature. *Building*
1011 *and Environment*, 90(0): 146-156.
1012

1013 **LIST OF FIGURE CAPTIONS**

1014 Figure 1. Study area: land uses in Kowloon peninsula and the Hong Kong Island.

1015 Figure 2. High spatial resolution thermal images acquired on Aug 5, 2013.

1016 Figure 3. Building heights of Kowloon peninsula and the Hong Kong Island.

1017 Figure 4. Relationships between the difference ($T_c - T_r$) and λ_p under four different
1018 daytime solar conditions.

1019 Figure 5. Relationship between the nighttime difference ($T_c - T_r$) and λ_p .

1020 Figure 6. Relationship between the daytime difference ($T_c - T_r$) and F under different
1021 solar conditions.

1022 Figure 7. Relationship between the nighttime difference ($T_c - T_r$) and F .

1023 Figure 8. Sensitivity of $T_c - T_r$ to irradiance: a) $T_c - T_r$ for cases 1 to 3 and; b) irradiance
1024 cases 1 to 3 as applied in a).

1025 Figure 9. Sensitivity of $T_c - T_r$ to wind speed under different conditions: a, $\lambda_p=0.2$,
1026 $H/L=2.5$; b, $\lambda_p=0.2$, $H/L=0.5$.

1027 Figure 10. Impact of material properties on daytime $T_c - T_r$: ($\max(T_c - T_r) - \min(T_c - T_r)$)
1028 obtained with the TUF – 3D numerical experiments and applying different combinations
1029 of material properties in Table 2. (the parameter values applying to each experiment are
1030 listed in the legend: H/L = ratio of building height to length; K_n = solar irradiance; θ_a =
1031 sun azimuth angle; θ_z = sun zenith angle; ω = wind speed)

1032 Figure 11. Impact of material properties on nighttime $T_c - T_r$: ($\max(T_c - T_r) - \min(T_c - T_r)$)
1033 obtained with the TUF – 3D numerical experiments and applying different combinations
1034 of material properties in Table 2. (the parameter values applying to each experiment are
1035 listed in the legend: H/L = ratio of building height to length)

1036 Figure 12. Scatter plot between actual and estimated T_c in the process of determining the
1037 coefficients: a, T_c from Eq. 8; b, T_c from Eq. 9.

1038 Figure 13. Comparison between T_c derived from T_r and T_c retrieved from component
1039 temperatures based on high resolution airborne thermal images: a, on Aug 5, 2013; b, Oct
1040 24, 2017.

1041 Figure 14. Radiometric, T_r , complete, T_c , surface temperature and their difference $T_c - T_r$
1042 retrieved from Landsat TM Band 6 in 2010 based on Eq.8.

1043 Figure 15. Nighttime T_r , T_c and their difference $T_c - T_r$ retrieved from ASTER image data
1044 in 2013 and GIS building based on Eq.9.

1045

1046